From Zn-Al LDH to ZIF-8@Zn-Al LDH conversion coatings on the surface of AA2024 alloy: Inside the process and the effect of the transformation on the protective properties

Valeryia Kasneryk [a],* , Eugen Gazenbiller [a] , D.C. Florian Wieland [b] , Vasil M. Garamus [b] , Maria Serdechnova [a] , Carsten Blawert [a] , Mikhail L. Zheludkevich [a,c]

[a] *Institute of Surface Science, Helmholtz-Zentrum Hereon, Max-Planck-Straße 1, 21502 Geesthacht, Germany*
[b] *Institute of Metallic Biomaterials, Helmholtz-Zentrum Hereon, Max-Planck-Straße 1, 21502 Geesthacht, Germany*
[c] *Institute of Materials Science, Faculty of Engineering, CAU Kiel University, Kaiserstraße 2, 24143 Kiel, Germany*

A B S T R A C T

Nowadays, interest in metal organic frameworks (MOFs) as potential materials for corrosion protection of aluminium alloys is increasing. However, application of MOFs in the form of conversion coatings remains limited due to challenging process of MOFs growth directly on Al based surfaces. This obstacle can be overcome by surface pretreatment that promotes further MOF formation. In the current investigation, Zn-Al LDH (layered double hydroxide) grown on the surface of AA2024 aluminium alloy was recrystallised into ZIF-8@Zn-Al LDH coating. *In situ* synchrotron and ex situ XRD analyses showed that recrystallisation of Zn-Al LDH into ZIF-8 was accompanied by intercalation of 2-methylimidazolate into the LDH gallery under the applied treatment conditions. Such a complex structure of the coating was beneficial for the corrosion protection of AA2024 alloy as the obtained coating contained an increased amount of 2-methylimidazole inhibitive species. Moreover, it was found that the variation of the treatment condition (95–140 °C, 3–24 h) affected the final performance of the ZIF-8@Zn-Al-LDH coating and the coating obtained at 95 °C for 12 h demonstrated the best performance.

1. Introduction

Aluminium and its alloys belong to the materials extensively used in industry, especially for aerospace, automotive and marine applications [1–3]. Such high interest is associated with a range of unique properties, including good strength-to-weight ratio as well as high damage tolerance [4–6]. However, Al-based surfaces face quite aggressive media, especially in marine or aerospace applications, and consequently can undergo fast corrosion degradation and loss of integrity. Due to those reasons, the development of novel approaches for efficient corrosion protection of aluminium and its alloys remains a relevant task.

In the last decade, metal organic frameworks (MOFs), a class of crystalline porous materials, were discovered as possible materials for effective corrosion protection of aluminium and its alloys [7]. This was possible thanks to the peculiar properties of MOFs, which include high surface area and porosity, tuneable pore size, and broad structure varieties [8–10]. Mostly, microcrystalline MOFs were applied as additives to polymers, where they were responsible for active corrosion protection

[7]. However, the mechanisms of corrosion protection by MOFs vary depending on their type. A quite specific way of corrosion inhibiting, which is inherent only to the MOF materials, is based on their structure's peculiarities. The ligands or metal cations forming MOFs can themselves act as corrosion inhibitors for Al-based substrates. In the corrosion process, MOFs decompose, which results in the release of inhibitors and protection of metallic surface [7]. In that context, MIL-47(V) encapsulated into epoxy-coating was reported to extend corrosion protection of the AA2024 alloy surface [11]. Furthermore, Zhang et al. reported the synthesis of BIPT-6 structure, which was specially designed for corrosion protection of AA2024 alloy. The high effectivity of BIPT-6 in inhibition was attributed to its structure, which was made of two types of inhibitors: Ce ions (III/IV) and 2,5-furandicarboxylate ligands.

Thanks to MOF porous structures, they can act as nanocontainers for loading corrosion inhibitors. Active nanocontainers represent nanomaterials that are capable of controllably storing/releasing of functional compounds on demand, for example, as a response to the presence of corrosive agents [12–16]. The released inhibitors can suppress corrosion

---

processes in damaged areas endowing the protective coatings with the ability of self-healing [13]. Such an approach can be exemplified by the work of Wei et al., who applied ZIF-8 loaded with 8-hydroxyquinoline (Q) as an additive to epoxy-coating for corrosion protection of AA2024 aluminium alloy [17]. Active protection was associated with a release of 8-hydroxyquinoline and 2-methylimidazole (2-HmIm) from Q@ZIF-8 in a response of the pH change during substrate corrosion. Other examples are the formation of pH-sensitive epoxy anticorrosion coatings loaded with benzotriazole (BTA) incorporated into Zn-BTC (BTC—benzenetricarboxylate) for aluminium protection [18] or sol–gel coating with BTA@ZIF-8 for protection of 1060 Al alloy [19]. Even more, BTA loaded into ZIF-8 and further incorporated into an acrylic coatings allowed not only to enhance protection of AA2024 aluminium alloy, but also introduce antibacterial properties into the system. It was related to the release of BTA, 2-HmIm and Zn^{2+} from BTA@ZIF-8 upon its decomposition [20]. Moreover, the nanocontainer function of MOFs was effective for the design of coatings with smart-sensing ability. The composite of Zr-MOF and rhodamine B (RhB) added into commercial epoxy resin coating demonstrated an ability to detect the damage to the coating surface and, consequently, the corrosion of Al substrate [21]. Such properties were reported to be associated with fluorescence properties and high selectivity of Zr-MOF@RhB toward Al^{3+}.

MOF additives can improve not only active protection ability, but also barrier properties of coatings. For example, addition of MIL-53 to silica sol–gel allowed to form more compact coating on the surface of AA2024 alloy due to the chemical interaction between MOF particles and the silica matrix (associated with esterification reaction with the free carboxylic groups of the MOF nanoparticles) [22]. Similarly, involvement of ZIF-8 to salicylaldehyde@ZIF-8/GO additive facilitated passive protection of AA2024 substrate coated with polyvinyl butyral (PVB) [23].

In addition to the involvement of MOFs as additives to polymers, MOFs can enhance the protective properties of metallic surfaces by being applied in the form of conversion layers. Up to now, this strategy has remained challenging, and the direct growth of MOFs as films on Al and its surfaces is still limited. However, this obstacle can be overcome via surface pretreatment facilitating further MOF formation. Thus, Zn-MOFs (ZIF-8 or Zn-MOF with 2,5-furandicarboxylic acid and BTA linkers) based coatings were obtained via controllable recrystallisation of Zn-Al LDH (layered double hydroxide) grown on Al plates [24,25] or 2A12-T4 Al alloy [26]. Formation of such coatings was possible due to the strong interactions between the MOF and the LDH structures [27, 28]. The obtained ZIF-8@LDH and Zn-MOF@LDH coatings showed high adhesion to the substrate and effective protection of Al-based substrates.

Other approaches for surface pre-modification are based on plasma electrolytic oxidation (PEO) or a combination of PEO and LDH surface treatment. The obtained coatings were successfully transformed into ZIF-8@PEO [29–31] or ZIF-8@LDH@PEO hybrid [32,33]. However, both strategies were successfully applied only for Zn [29,30] and Mg [31–33] based alloys, but no investigations involving Al-based surfaces have been reported up to now.

Summarising all aspects addressed previously, it should be mentioned that regardless of the investigation focused on different MOF types for corrosion protection of Al-based surfaces, their implementation in the form of conversion coatings is still limited and has been reported only in a few studies. Even more, there is a knowledge gap in understanding how the MOF formation runs on the alloys surfaces. The current investigation aims to understand the transformation mechanism of Zn-Al LDH grown on the surface of AA2024 aluminium alloy into ZIF-8. ZIF-8 is known as water stable MOF [34–36]. For that purpose, the process was followed *in situ* by synchrotron XRD analysis on the metallic surface. The second part of the current work aimed to investigate the protective ability of the obtained ZIF-8 containing coatings and how they are affected by the treatment conditions.

2. Experimental part

2.1. Materials

2.1.1. Substrate

As a substrate material, AA2024 aluminium alloy was used with the following nominal composition according to spark analysis (Spectrolab M9, Ametek-Spectro, Germany): 93.18 % Al, 4.65 % Cu, 1.42 % Mg, 0.44 % Mn, 0.10 % Si, 0.09 % Fe, 0.03% Ti, 0.04 % Zn, 0.02 % Cr. The samples were cut into 20 mm × 30 mm × 1.6 mm plates. Before forming the Zn-Al LDH coatings on the AA2024 surface, they were ground with #1200 and #2500 grades of silicon carbide paper, rinsed with deionised water, and dried at 25 °C under air.

2.1.2. Synthesis of Zn-Al LDH coating on the surface of AA2024 alloy

The Zn-Al LDH coating was grown on the surface of AA2024 aluminium alloy according to the procedure described previously [37, 38]. Briefly, the synthesis was carried out from a reaction mixture containing 0.1 M zinc nitrate ($Zn(NO_3)_2 \cdot 6H_2O$, Alfa Aesar, 98 %) and 0.6 M ammonium nitrate (NH_4NO_3, Aeros Organics, 99+%) at 95 °C for 30 min. pH was adjusted to 6.4 by the addition of NH_4OH (Thermo Fisher Scientific, 28–30 %). Aluminium needed for the formation of Zn-Al LDH was provided into the reaction mixture upon the AA2024 alloy dissolution. After the Zn-Al LDH conversion coating was formed, specimens were rinsed with deionised water and dried under atmospheric conditions for 12 h. For the *in situ* synchrotron investigation of Zn-Al LDH transformation into ZIF-8, obtained specimens were cut into 5 mm × 10 mm.

2.1.3. Partial recrystallisation of Zn-Al LDH CC into ZIF-8

To form ZIF-8 on the surface, AA2024 alloy plates coated with Zn-Al LDH CC were treated with 25 ml of 0.25 M 2-methylimidazole ($CH_3C_3H_2N_2H$, Acros Organics, 99 %) solution in methanol (CH_3OH, Roth, ≥99.5 %) in 125 ml autoclave at 95–140 °C for 3–24 h. After the treatment the specimens were washed with ethanol (C_2H_5OH, Roth, ≥99.5 %) and dried at 23 °C for 16 h. The final samples were titled as *T-t*, where *T* refers to the treatment temperature: 95, 110 or 140 °C, respectively, and t corresponds to the treatment time of 3, 6, 12 or 24 h.

2.2. Characterisation of the obtained materials

The phase composition of parental Zn-Al LDH and ZIF-8@LDH coatings was evaluated by X-ray diffraction (XRD, D8 Advanced Powder diffractometer, Bruker, Germany) with Ni-filtered Cu *K*α radiation. The measurements were performed at a glancing angle of 3°, a scan range from 5 till 60°, a step size of 0.02° and a scan speed of 1 s per step.

The process of Zn-Al LDH into ZIF-8 transformation was followed *in situ* at the P08 high-resolution diffraction beamline of the PETRA III synchrotron radiation source (DESY, Hamburg, Germany). The X-ray energy was 25 KeV, the beam size was 2 μm × 30 μm focused by refractive lenses, the incident angle value was 0.12° θ). A 2D PERKIN Elmer detector with a 200 μm pixel size was used. The distance to the detector was 1012 mm. Calibration of the sample to detector distance and beam centre was done by using a LaB6 standard. Data reduction was done using pyFAI [39]. The diffraction data analysis was performed using an in-house developed Matlab routine. It should be noted that the XRD patterns from the synchrotron beamtime were recalibrated to 8 keV for better comparability to lab experiments. As the temporal evolution of the phase composition of the layers was observed, an exposure time of 5 s per frame was used, which was the best compromise between the temporal resolution and the signal strength. The experimental setup included a custom-built *in situ* cell with windows made of 100 μm thick Kapton, allowing for grazing incidence X-ray diffraction measurements (Fig. 1). The cell's body consists of polyether ether ketone (PPEK). A PT-1000 temperature sensor, fully encapsulated by a polymer coating, is in direct contact with the solution to allow for exact temperature
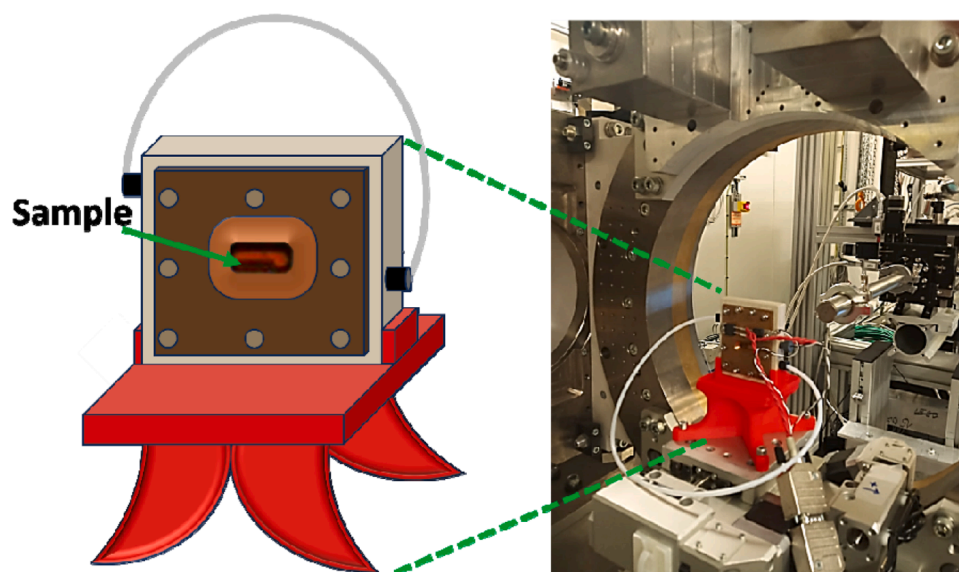
Fig. 1. The closed *in situ* cell used for the synchrotron analysis of the Zn-Al LDH into ZIF-8 transformation process: the schematic representation and photo of the cell installed at P08 DESY station.

control. Heating elements were placed outside the cell, which was brought completely to 95 °C. Thus, the cell was constructed in a way that no metal was in contact with the solution and specimens. During the experiment, the specimens were treated with 5 ml of 0.25 M 2-HmIm in methanol at 95 °C and the process was followed for 8540 s. The data accumulation was started after the reactor reached the temperature of 95 °C, which was considered as the starting time (0 s). It should also be mentioned that the results obtained in the frame of the current work are specific to this experimental setup (Fig. 1) in terms of cell geometry etc.

Raman spectroscopy was used for further structure analysis (Bruker, Senterra, Germany). The data were acquired under the following parameters: 532 nm laser wavelength, 20 × objective lens, 25 mW of laser power, 50 μm aperture size, and 64 scans with an integration time of 4 s. The obtained Raman spectral data were evaluated by Bruker OPUS 7.5.18 software. Further structure analysis was performed by FTIR spectroscopy using a Bruker TENSOR 27 FTIR spectrometer equipped with an ATR facility.

Scanning electron microscopy (SEM, Tescan Vega3 SB, Czech Republic) in combination with an energy dispersive X-ray spectrometry (EDS, Ultim Max 40 Oxford, UK) was applied to analyse surface morphology and cross-sections of Zn-Al LDH and ZIF-8@LDH coatings. Surface morphologies were observed in secondary electron (SE) mode, while cross-sections were evaluated in back scattered electron (BSE) mode. Data acquisition was performed with high voltages of 8.0–15.0 kV and beam intensity of 7.0–14.0. To perform the analysis of cross-sections, the AA2024 plates coated with Zn-Al LDH or ZIF-8@Zn-Al LDH were embedded in resin, ground by silicon carbide paper (#1200, #2500, #4000), rinsed with deionised water and dried with air. Finally, embedded samples were spattered with carbon. The size of the LDH and ZIF-8 crystals was estimated from the SEM micrographs using ImageJ software [40].

The corrosion protective ability of Zn-Al LDH or ZIF-8@LDH coating formed on AA2024 alloy was evaluated by electrochemical impedance spectroscopy (EIS) in a naturally aerated 0.5 wt.% NaCl solution at 25 °C for 7 days using a Gamry 1000 potentiostat (USA) and compared with the bare substrate. The experiments were carried out in a conventional three-electrode cell with a platinum counter electrode, a saturated Ag/AgCl reference electrode, and coated or bare AA2024 metallic plate as a working electrode. The exposed area on the AA2024 plates and the coated one was 0.5 cm^2. The analysis was performed over a frequency range from 100 kHz to 0.01 Hz at open circuit potential (OCP), with 10

mV RMS sinusoidal potential perturbations. The experiments were repeated for three times for each of the specimens to check reproducibility of the results. After 7 days of the EIS measurements, the surface of corrosion products was studied using SEM. Distribution of relaxation times was done using Gamry Echem Analyst 2 with a regularisation parameter of 1.0000×10^{-4}. The ZView software, version 3.3c (Scribner, North Carolina, USA) was used to fit the impedance data. Additionally, to identify the corrosion products for the bare AA2024 specimen and the one coated with Zn-Al LDH and ZIF-8@LDH (95-12h), the specimens were immersed into 0.5 wt.% NaCl solution at 25 °C for 7 days (similar to EIS conditions) and after that characterised using XRD and Raman spectroscopy. The potentiodynamic polarization was recorded at a sweep rate of 1 mV/s from −1.0 V to 1.0 V vs OCP after immersion of the specimens into 0.5 wt.% NaCl solution at 25 °C.

3. Results and discussion

3.1. Ex-situ XRD study of Zn-Al LDH into ZIF-8 transformation

In the current work, the formation of ZIF-8@Zn-Al LDH conversion coatings on the surface of AA2024 aluminium alloy was in focus. The coatings were formed via partial recrystallisation of pre-formed Zn-Al LDH, where Zn^{2+} ions needed for the formation of ZIF-8 structure were delivered exclusively from LDH, i.e. no additional source of Zn was involved. To understand how Zn-Al LDH rearranges into ZIF-8 structure and which parameters affect this process, firstly, temperature and time of the post-modification were systematically varied.

Fig. 2 represents the XRD patterns of the initial Zn-Al LDH coatings and three batches of the ZIF-8@LDH specimens obtained at 95, 110 and 140 °C. The pattern of the parental Zn-Al LDH corresponds to Zn$_2$Al (OH)$_6$NO$_3$·1.9H$_2$O LDH single phase (PDF: 00-055-0193) with high crystallinity. After the treatment with methanolic solution of 2-HmIm, ZIF-8 phase (PDF: 00-062-1030) was formed on the surface, whose reflections can be clearly followed in the spectra of ZIF-8@Zn-Al LDH samples. Both parameters, temperature and time, had an impact on the recrystallisation process. The increase of temperature from 95 till 110 °C accelerated ZIF-8 crystallisation (for 3–12 h), which can be seen from, Fig. 2c) and f) demonstrating the evolution of the intensities for ZIF-8 (011) reflections normalised to (111) Al reflection (the reflection from the AA2024 substrate; the full ranges of XRD are presented in SI, Fig. SI1). Further increase of the treatment time up to 140 °C did not
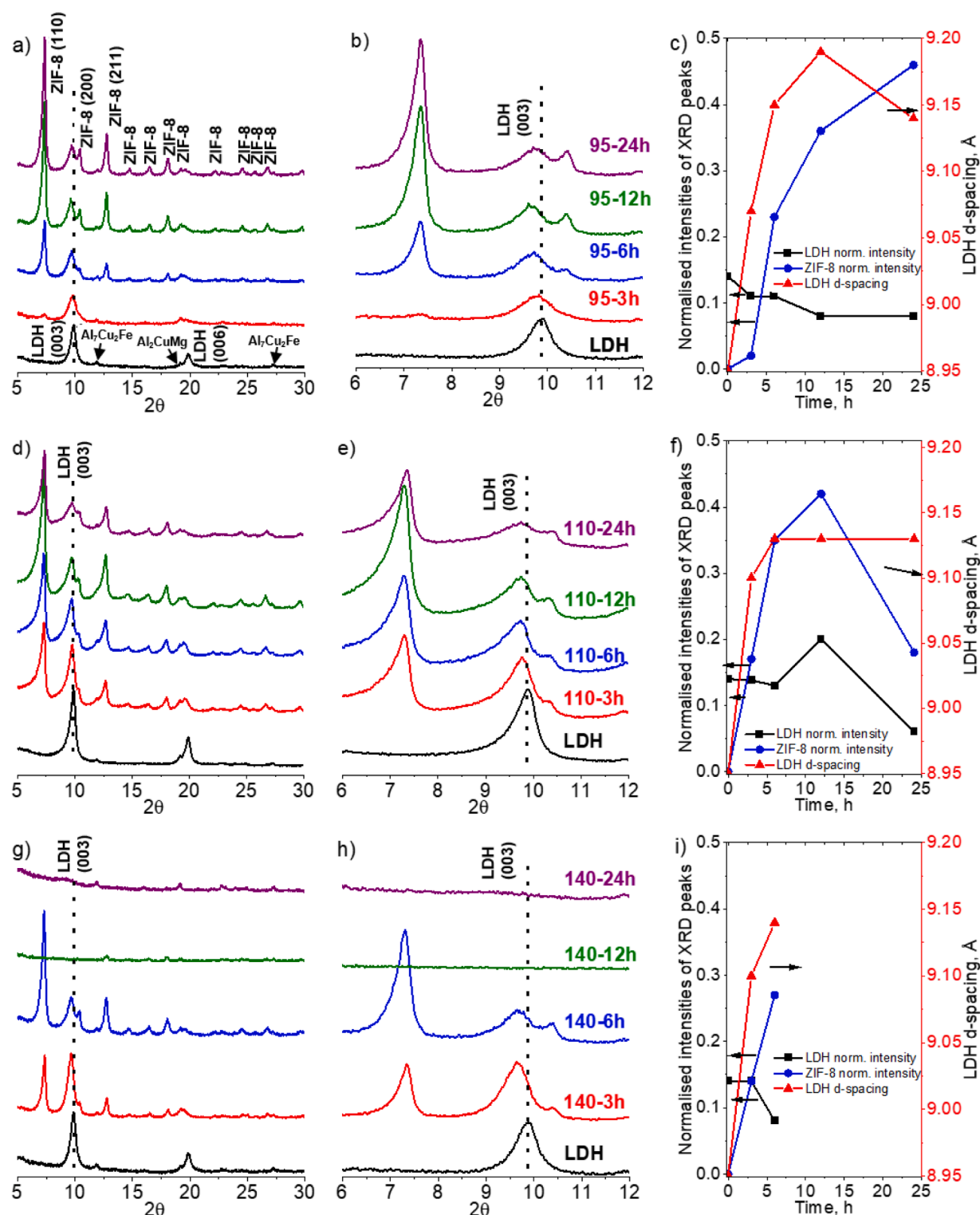
Fig. 2. XRD patterns of the ZIF-8@LDH coatings on AA2024 obtained under different conditions: a–c) 95 °C, d–f) 110 °C, g-i) 140 °C. c, f, i) represents evolution of intensities of the XRD peaks for ZIF-8 (011), Zn-Al LDH (003) normalised to (111) Al reflection and evolution of the LDH d-spacing with time. Al$_7$Cu$_2$Fe and Al$_2$CuMg are originated from AA2024 substrate. The full range of the XRDs is presented in Fig. SI1.

positively affect ZIF-8 formation. Based on Fig. 2g)–h), for 140-3h and 140-6h specimens, reflections corresponding to ZIF-8 phases were characterised by lower intensities comparing to the 110-3h and 110-6h samples, respectively. Several observations should be mentioned, when discussing the effect of the treatment time. Firstly, regardless of the temperature applied, the intensity of the signals corresponding to ZIF-8

increased with the prolongation of the treatment from 3 to 12 h (for 140-t batch from 3 to 6 h), while the Zn-Al LDH peaks intensities slowly declined, indicating its partial decomposition. Further prolongation of the synthesis till 24 h positively affected the ZIF-8 formation at 95 °C and the coating exhibited an XRD pattern with increased intensities of the MOF phase. In contrast, the 110-24h sample intensities of both

phases ZIF-8 and LDH were decreased. Moreover, long-term treatment at 140 °C resulted in total degradation of the coatings, as neither ZIF-8 nor Zn-Al LDH were detected for 140-12h and 140-24h coatings. This indicates that elevated temperatures and long-term treatments were not suitable for the formation of ZIF-8@LDH coating on the surface of AA2024 alloy. Such observation can be related to the acceleration of LDH structure dissolution at elevated temperatures similar to one reported in [41,42]. In turn, released Zn^{2+} might have reacted with 2-HmIm linkers forming ZIF-8, but mainly in powder form and not a coating on the surface of AA2024 alloy.

Surprisingly, it was found that the process of Zn-Al LDH-to-ZIF-8 transformation was accompanied by the intercalation of 2-HmIm organic linker into the LDH gallery. LDHs as materials are known for their ion-exchange ability, thanks to that, a range of active species can be intercalated into the structure [13,14,43–46]. However, as it was demonstrated for Zn-Al LDH grown on the surface of AA2024 alloy, intercalation of inhibitors is typically carried out at temperatures lower than 95 °C from water solutions. In turn, in the frame of this investigation, it was observed that intercalation of 2-HmIm can occur at elevated temperatures, 110 and 140 °C in methanol. As it can be seen from Fig. 2, the (003) reflection of LDH was shifted into the area of lower 2θ angles for all three batches of samples. For the specimens treated at 95 °C, the values of corresponding d-spacings increased from 9.07 to 9.19 Å with the prolongation of the treatment time from 3 to 12 h, vs. 8.95 Å for the parental LDH. But the specimen treated for 24 h exhibited a lower d-spacing, namely 9.14 Å. In case of the 110-t series, d-spacing reached the value of 9.13 Å after 6 h of the treatment and did not changed further, when the treatment time was increased to 12 and 24 h, respectively. At 140 °C the maximum d-spacing of 9.14 Å was seen for the 140-6h coating. It should also be mentioned that for all *T-t* specimens, the peaks corresponding to the (003) reflections were much broader and had shoulders in the region of lower 2θ angles. Therefore, it can be assumed that partial NO_3^--to-2-mIm$^-$ ion exchange took place under the applied conditions, i.e. both ions are located in the LDH interlayer space, similarly to the intermediate phase detected during intercalation of anions species into Zn-Al LDH-NO_3^- reported in [47]. Besides, complete intercalation under applied conditions is most likely restricted due to the parallely running process of ZIF-8 crystallisation and spatial/mechanical limitations.

3.2. In situ synchrotron investigation of Zn-Al LDH into ZIF-8 transformation

Ex situ XRD analysis allows to follow the phase composition of the final coatings, i.e. obtained after a certain treatment time, washed and dried. However, it is limited to track any intermediate phases, which are unstable and formed mainly during the first several hours of the treatment. To delve deeper into the recrystallisation of Zn-Al LDH into ZIF-8 in methanolic solution of 2-HmIm, the process was followed *in situ* by synchrotron X-day diffraction at 95 °C for 8540 s. The time evolution of the XRD patterns during the transformation is presented in Fig. 3. The data acquisition was started after the temperature of the reaction
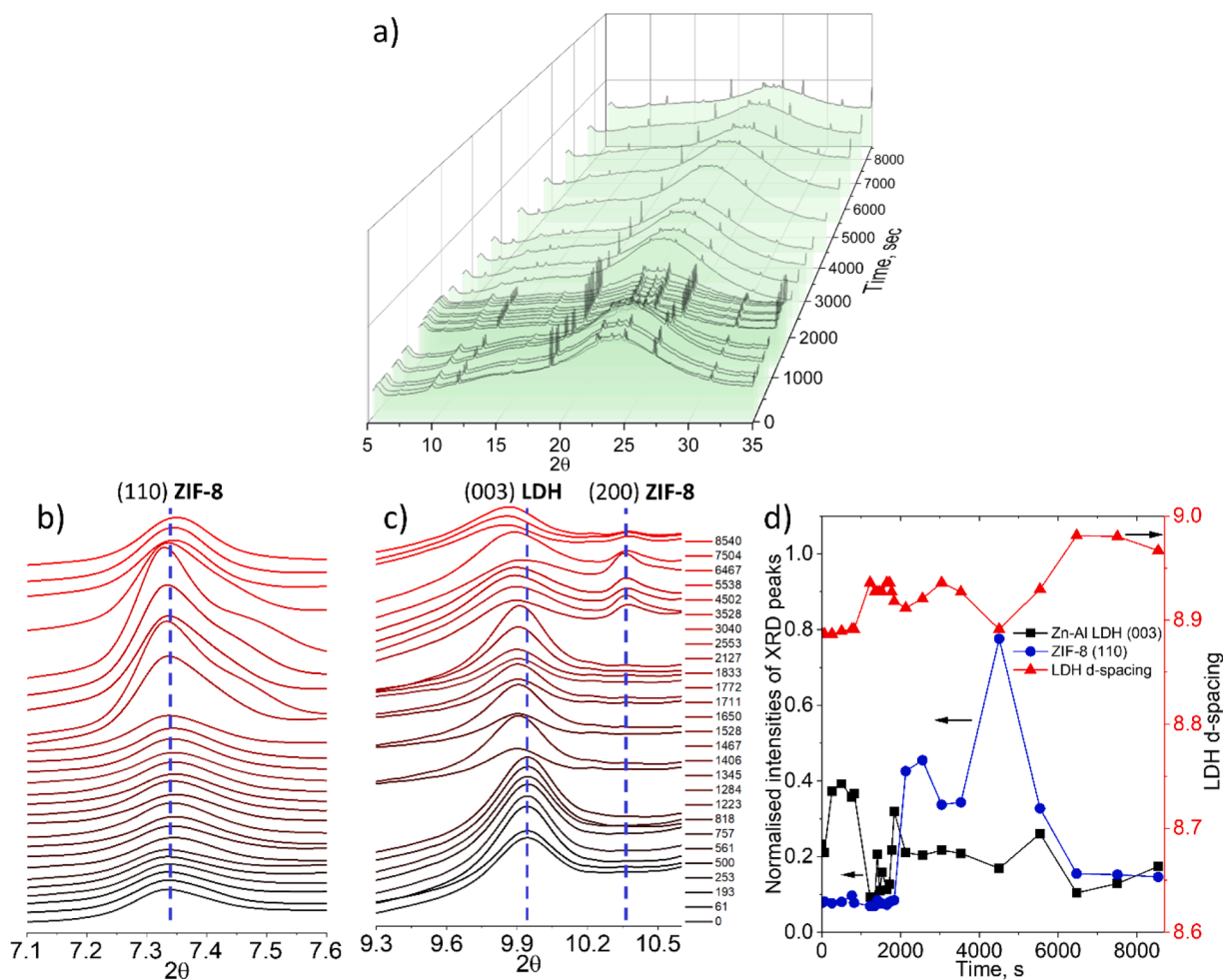
Fig. 3. a) Evolution of XRD patterns during the treatment of Zn-Al LDH grown on AA2024 alloy with 0.25 M 2-HmIm in methanol at 95 °C, b)-c) selected regions demonstrating evolution of ZIF-8 (011), Zn-Al LDH (003) and ZIF-8 (200) reflections, respectively. d) evolution of normalised intensities of ZIF-8 (110) Zn-Al LDH (003) reflections and LDH d-spacing with time.

mixture reached 95 °C, which took around 2 min. This time was taken as a starting point, i.e. 0 s. However, immediately after the starting of the data acquisition, the presence of low-intensive reflections corresponding to ZIF-8 phase was detected. It can be seen from Fig. 3b), exhibiting the evolution of the (110) ZIF-8 reflection. Such observation can indicate that the recrystallisation of Zn-Al LDH into ZIF-8 runs relatively fast and at lower temperatures. It agrees with the data of Wu et al., who demonstrated that Zn-AlLDH@ZIF-8 powder can be synthesised at room temperature [48].

In situ synchrotron measurements confirmed that LDH-to-ZIF-8 recrystallisation and intercalation of 2-HmIm linker into Zn-Al LDH gallery take place simultaneously under the treatment conditions. It corresponds to the results of ex situ XRD analysis discussed previously. The intensity of the (110) ZIF-8 reflection remains low for 0–1833 s, after 2127 it started to increase, indicating a more active crystallisation of ZIF-8. It reached the maximum value after 4502 s, which can be easily followed from Fig. 3d), representing the evolution of normalised intensities of (110) ZIF-8 reflection. After 4502 s the intensity of the (110) reflection decreased, but still the values were higher than those at the beginning of the treatment (normalised intensities, 0.15–0.33 vs. 0.069–0.085 for the spectra after 5538–8540 s and 0–1833 s, respectively). Moreover, the signal at 10.39° 2θ corresponding to the (200) reflection of ZIF-8 (Fig. 3c)) was not visible in the XRD patterns for 0–1837 s. It became remarkable only after 2127 s of the treatment. Its intensity increased with prolongation of the treatment till 4502 s, and further dropped. It can be associated with formation and further partial dissolution of ZIF-8 crystals from the surface at the beginning of the process as well as possible crystal detachment into the treatment bath.

Fig. 3c) depicts the changes of the (003) LDH reflection. From the beginning of the analysis till 818 s, no changes in the positions or the peak intensities were found (Fig. 3d), Table SI1). However, the intensity of this reflection dropped after 1223 s of the transformation, as well as the position was slightly shifted to lower angles, indicating an increase of the d-spacing caused by the started intercalation of the organic linker. Interestingly, in the period from 1223 s till 5538 s, LDH intensities permanently dropped and increased as well as the *d*-spacings slightly diminished and rose. It can be proposed that in that period, the LDH partially dissolves and crystallises again, being intercalated by nitrate or 2-mIm⁻. It should be mentioned that *d*-spacings obtained by the *in situ* synchrotron analysis did not reach the d-spacing values calculated based on the results of ex situ XRD, which was related to the different times of both analysis. While for the *in situ* synchrotron the data were obtained for 0–8540 s, the first sample tested by ex situ XRD was obtained for 10800 s (3 h). Moreover, although in both cases, the Zn-Al LDH transformation was followed at 95 °C, the reactors had different volumes (125 ml autoclave vs. 5 ml for the *in situ* cell).

Discussing the possible intermediate products formed in the process of Zn-Al LDH transformation with 2-HmIm, the presence of the shoulder at 7.46° 2θ can be noticed in the XRD patterns in the time period from 2127 till 5538 s (Fig. 3b). This signal is not characteristic neither for ZIF-8 nor for LDH phases. However, it can be assumed that it could correspond to some unstable intermediate products of ZIF-8 formation similarly to $C_{32}H_{40}N_{16}Zn_4$ [29], as it appeared in the stage, when ZIF-8 phase started to be actively crystallised on the surface and disappeared together with a drop of the MOF phase.

The last observation, which should be taken into account, is the presence of halos in the range from around 12 to 35° 2θ in most of the patterns. Generally, such halos are characteristic of amorphous phases present in the samples. However, it can also originate from the scattering of the solvent used for the reaction, in this case methanol. As it was demonstrated by Klimakow et al. who followed the evaporation of methanolic solutions of nifedipine, similar halos were detected in the XRD patterns of the methanolic solutions before evaporation [49]. Moreover, De Matos et al. also observed such a halo during the process of crystallisation of piracetam from methanolic solution [50]. In that context, the experimental conditions do not allow clear distinction of the

exact reason for the presence of this halo in the patterns presented in Fig. 3a). Regardless of the fact that it is most likely related to the methanolic media, the formation/dissolution of the amorphous phase during the transformation can not be fully excluded. It should be also mentioned that the halo was less remarkable in the spectra after 1223–1833 s of the treatment, which was most probably related to regularly performed beam alignment during the experiment.

3.3. Structural analysis of ZIF-8@LDH coating on AA2024 aluminium alloy by Raman and FTIR-ATR spectroscopy

The surface modifications taking place in the process of Zn-Al LDH-to-ZIF-8 transformation were further tracked using Raman and AFR spectroscopy (Fig. 4). The Raman spectrum of initial Zn-Al LDH (Fig. 4a)) demonstrates the presence of a highly intensive signal at 1055 cm⁻¹ corresponding to NO_3^{2-} stretching modes and bands at 487 and 549 cm⁻¹ associated with stretching vibrations of Al—O—Al and Zn—O—Al [51], respectively. Additionally, the presence of a low intensive signal at 716 cm⁻¹ is observed in the spectra of Zn-Al LDH, which most likely corresponds to CO_2 adsorbed from the air [51]. After the treatment with methanolic solution of 2-HmIm, additional bands corresponding only to the ZIF-8 structure appeared in the spectrum. The most intensive signals were located at 1508, 1460, 1146, 686 and 178 cm⁻¹ which are typical for C—C stretching, CH_3 bending, C—N stretching, imidazole ring puckering and Zn—N stretching, respectively [52–54] and correspond to the ZIF-8 structure.

Similar results were obtained by AFR spectroscopy (Fig. 4b)). The broad bands on the spectra of both LDH and ZIF-8@LDH located at 3700–2900 cm⁻¹ related to the hydroxyl stretching vibrations in LDH layers and H_2O molecules [55]. The IR band at 1646 cm⁻¹ corresponds to the bending vibration of the interlayer water [56]. The signal belonging to NO_3^- intercalated into the LDH are located in the region of 1404–668 cm⁻¹: 1404 and at 1382 cm⁻¹ – the anti-symmetric stretching modes (ν_{3b} and ν_{3b}), 822 cm⁻¹ – out-of-plane symmetric deformation mode (ν_2) and 668 cm⁻¹ – the anti-symmetric deformation mode (ν_4) [56,57]. Similarly to the results of the Raman spectroscopy, after partial recrystallisation of Zn-Al LDH into ZIF-8, presence of additional IR bands corresponding to the ZIF-8 structure was observed. The IR band at 2930 cm⁻¹ is associated with the C—H symmetric stretch of the methyl group, while at 3138 cm⁻¹ with =C—H stretch for the aromatic ring. The signal at 1587 cm⁻¹ corresponds to the C=N stretching. The IR peaks located in the region of 900–1350 cm⁻¹ are attributed to the in-plane bending of the imidazole ring, while out-of-plane bending of the ring are responsible to signals below 800 cm⁻¹. The high intensive signal at 1146 cm⁻¹ is assigned to =C—H bending [58,59].

3.4. Characterisation of surface morphology and elemental composition of ZIF-8@LDH coatings using SEM/EDS

The batch of the specimens obtained at 95 °C was in the focus of further characterisation. 110-6h and 140-6h coatings were studied to compare the impact of the transformation temperature on the final properties. Moreover, the 140-12h specimen was evaluated to understand the processes taking place on the surface during the treatment at high temperatures. Figs. 5 and SI3 depict the SEM top view of the parental Zn-Al LDH and ZIF-8@LDH coatings grown on the surface of AA2024 aluminium alloy. Moreover, Fig. SI3 represents the elemental compositions in different regions of the coatings. The initial Zn-Al LDH CC demonstrates the surface morphology typical for Zn-Al LDH grown on the surface of AA2024 alloy [37,38,60]. It is characterised by a homogenous coverage with thin LDH flakes with a size of 0.5–2 × 0.05–0.15 μm. Flower-like agglomeration of the LDH crystals were also present on the surface, which are mainly formed around Cu-rich intermetallics as it was reported in our previous investigations [61]. The thickness of the coating was 1.0–2.1 μm (Fig. SI2) based on the analysis of the cross-sections. Mapping of the elemental distribution showed that
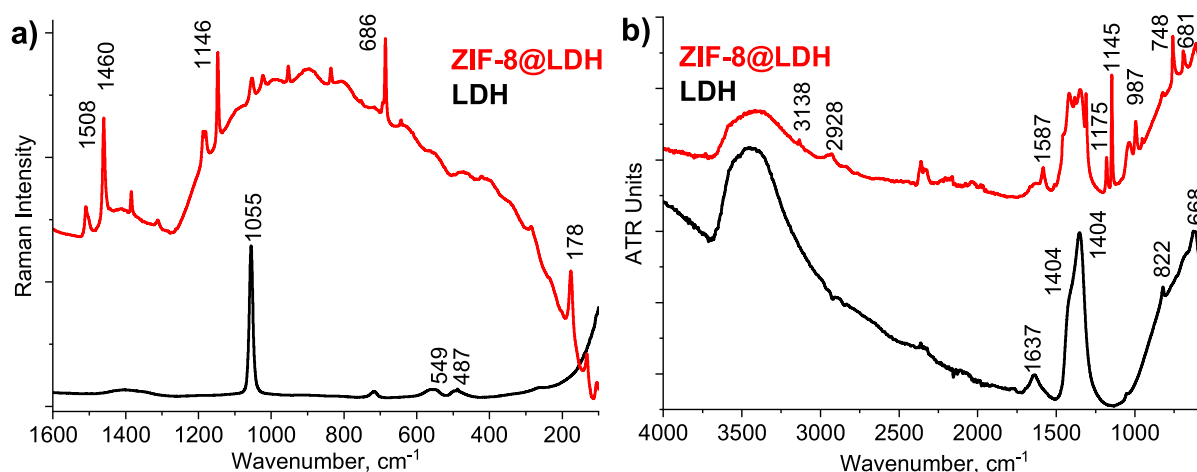
Fig. 4. a) Raman and b) FTIR-ATR spectra of the parental Zn-Al LDH CC on AA2024 aluminium alloy and ZIF-8@LDH coatings.

the initial LDH coating was characterised by homogenous distribution of Zn, Al and O through the coating thickness. However, the line scan through the coating thickness showed that the concentration of Zn and O had the highest value in the middle of the coating.

The surfaces of the 95-t coatings remained homogenous, similar to the initial Zn-Al LDH CC. Moreover, several cracks were found on the surface of 95-3h and 95-6h around or on the "flower"-areas, that can be seen from the left insert of Fig. 5b). The main differences between 95-t specimens were in the morphology of the crystals located on the surface. Thus, the high magnification SEM micrograph of 95-3h (Fig. 5b, right insert) reveals that the AA2024 surface is mainly covered with tiny LDH flakes like the parental Zn-Al LDH CC. Moreover, a few not-well-shaped cubic-like ZIF-8 crystals with a size of 0.3–0.5 μm can be depicted. Further prolongation of the treatment to 6 h (i.e. 95-6h, Fig. 5c) led to the increase of the number of ZIF-8 crystals as well as their enlargement up to 0.5–0.9 μm. Moreover, the increase of the crystals amount on the surface results in the beginning of the sealing of intercrystalline porosity of LDH, i.e. pores between LDH flakes located on the surface. Similar trends in enlargement and increase of the amount of ZIF-8 crystals were observed when the reaction time was further increased to 12 and 24 h. Thus, the crystals were characterised by the size up to 1.2 and 3 μm for 95-12h and 95-24h specimens, respectively. In both cases, ZIF-8 crystals homogenously covered the LDH surface and healed most of the surface defects. However, only the specimen obtained for 24 h was characterised by the covering with well crystallised ZIF-8 crystals with rhombic dodecahedron morphology. Moreover, it should be also noted that the long-term treatment (i.e., 95-24 h) led to the cracking of ZIF-8 crystals associated with a stress in the layer emerging due to the crystals' growth on the surface in all directions. A similar effect was observed previously in the process of long-term crystallisation of ZIF-8 on the surface of PEO coating on Z1 Zn alloy [30]. Besides, these cracks represent additional surface defects and can adversely affect the final coating properties, e. g. corrosion resistance. Prolongation of the treatment also affected the thickness of the entire coatings and while for 95-6h it was 1–1.5 μm (comparable to the starting LDH), the value increased up to 2.4 μm for 95-24h (Fig. SI2) based on cross-section SEM analysis. However, cross-sectional analysis did not allow to clearly distinguish LDH and ZIF-8 layers, which was probably associated with crystallisation of ZIF-8 through the whole LDH coating but not only on the top surface.

An increase of the temperature of the process negatively impacted the surface and crystals morphology of the final coatings. Thus, while 110-6h specimen was also characterised by the homogenous surface coverage, the high magnification SEM micrograph demonstrates the presence of surface cracks (Fig. 5f)). In case of further heating till 140 °C (i.e. 140-6h, Fig. 5g)), the surface appeared uneven with regions, where the initial coating was peeled-off. In both cases, the surfaces looked like

the one covered by the agglomeration of ZIF-8 crystals sintered together, whose size can hardly be estimated. SEM analysis of the 140-12h specimen showed that the surface of this coating was fully peeled-off after the treatments and no evidence of the presence of LDH flakes on the surface was detected. Moreover, low-magnification SEM pictures demonstrated the presence of agglomeration of not well-shaped ZIF-8 crystals with a size of 1–5 μm was detected.

The SEM results also correlate with EDS mappings displayed in Fig. 6. The initial Zn-Al LDH was characterised by the inhomogeneous distribution of Al, Zn, O and N. The "flower" zones were enriched with Zn and O, that correlates with results of the chemical analysis presented in Fig. SI3. Thus, these "flowers" were made of 36.3 ± 0.6 % Zn, 36.8 ± 0.6 % O and 21.2 ± 0.4 % Al, while LDH flakes zone was composed of 20.0 ± 0.5 % Zn, 26.2 ± 0.5 % O and 49.2 ± 0.6 % Al. EDS mapping for 95-3h and 95-6h showed that these coatings retain the distribution of Al, Zn an O on the surface similar to parental Zn-Al LDH. Moreover, the presence of the spots enriched with N and C was detected, whose amount was higher for 95-6h. Being the main elements of the 2-mIm$^-$ linker from ZIF-8, the presence of N and C confirms crystallisation of the ZIF-8 phase on the coatings surface. In the case of these coatings, flower-like areas detected on the surface were also mainly made of Zn (Fig. SI3, 39.3 ± 0.6 % and 31.0 ± 0.6 % for 95-3h and 95-6h, respectively). Moreover, the presence of C was also found, whose amount was higher for 95-6h (9.3 ± 0.7 vs. 30.9 ± 0.7 %), which correlates with a presence of a higher amount of ZIF-8 crystals on the surface for this specimen. Analysis of 95-12h, 95-24h and 110-6h specimens demonstrated that Zn, N and C were uniformly located on the surface of AA2024 alloy except for the areas of numerous streaks, which were characterised by high concentrations of Al and O (Fig. 6). These enriched Al and O streaks were located between the ZIF-8 crystals or in the surface cracks. Chemical analysis of these specimens in different regions of the coatings showed that in all cases coatings were characterised by increased concentration of C, confirming crystallisation of a higher amount of ZIF-8 phase on the surface. In case of 140-6 h specimen, similar Al-based streaks can be seen, but their sizes were smaller than for other coatings, which is most likely associated with crystals' sintering mentioned previously. Moreover, chemical analysis of different regions of this coating demonstrated, while the area covered by LDH and ZIF-8 crystals was characterised by a composition comparable to other ZIF-8@LDH coatings, the region of the coating, which was peeled-off, was mainly composed of Al (84.1 ± 1.5 %). EDS mapping of the specimen treated at 140 °C for 12 h clearly indicates the presence of 2 zones: the one enriched with Al and O inclusions and the one with high concentration of Zn, N and O, which also agrees with compositions presented in Fig. SI3. Such observation indicates that the surface of AA2024 was fully peeled-off after the treatment for 140 °C for 12 h. However, ZIF-8 phase
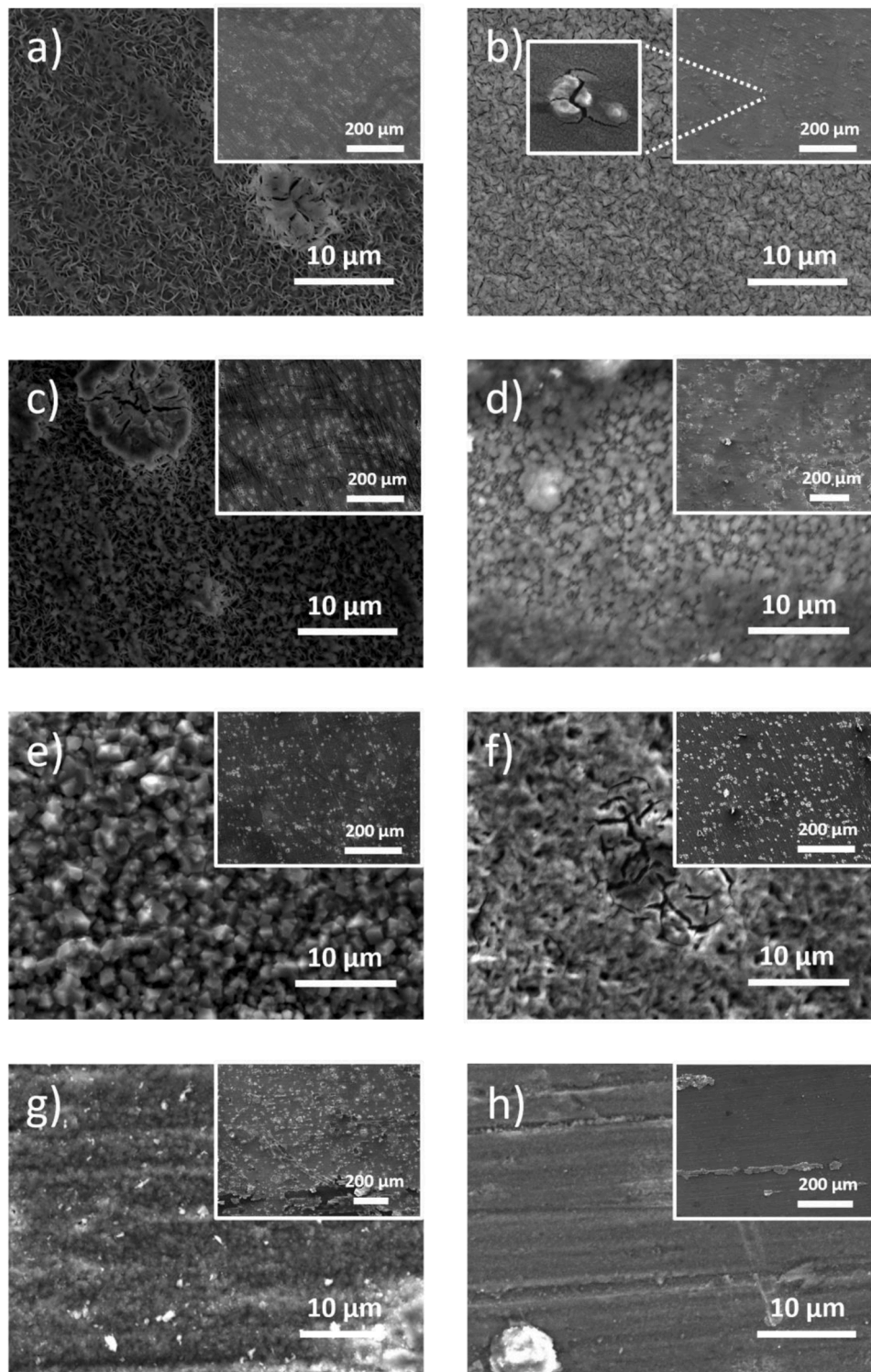
Fig. 5. SEM micrographs of AA2024 samples covered with a) parental Zn-Al LDH, b) 95-3h, c) 95-6h, d) 95-12h, e) 95-24h, f)110-6h, g)140-6h, h) 140-12h.

was also formed under the applied conditions and ZIF-8 crystals were further randomly deposited on the surface of AA2024 alloy. However, no homogeneous covering of the surface with ZIF-8 crystals was achieved. Due to that reason, no presence of ZIF-8 phase was detected by the XRD analysis (Fig. 2).

Summarizing the results of SEM and EDS, it can be concluded that both increased temperatures and prolonged treatment time had adverse effects on the surface and crystal morphology of the final coatings and both parameters must be controlled to design a coating with high protection properties.

3.5. Corrosion protection ability

The corrosion resistance of ZIF-8@LDH coatings was evaluated using electrochemical impedance spectroscopy (EIS) and compared with Zn-Al LDH coated and bare AA2024 alloy. Fig. 7 exhibits the Bode plots and phase angle plots after 1, 24 and 168 h immersion of the specimens into 0.5 wt.% NaCl solution. Fig. 7h) represents how the impedance modulus
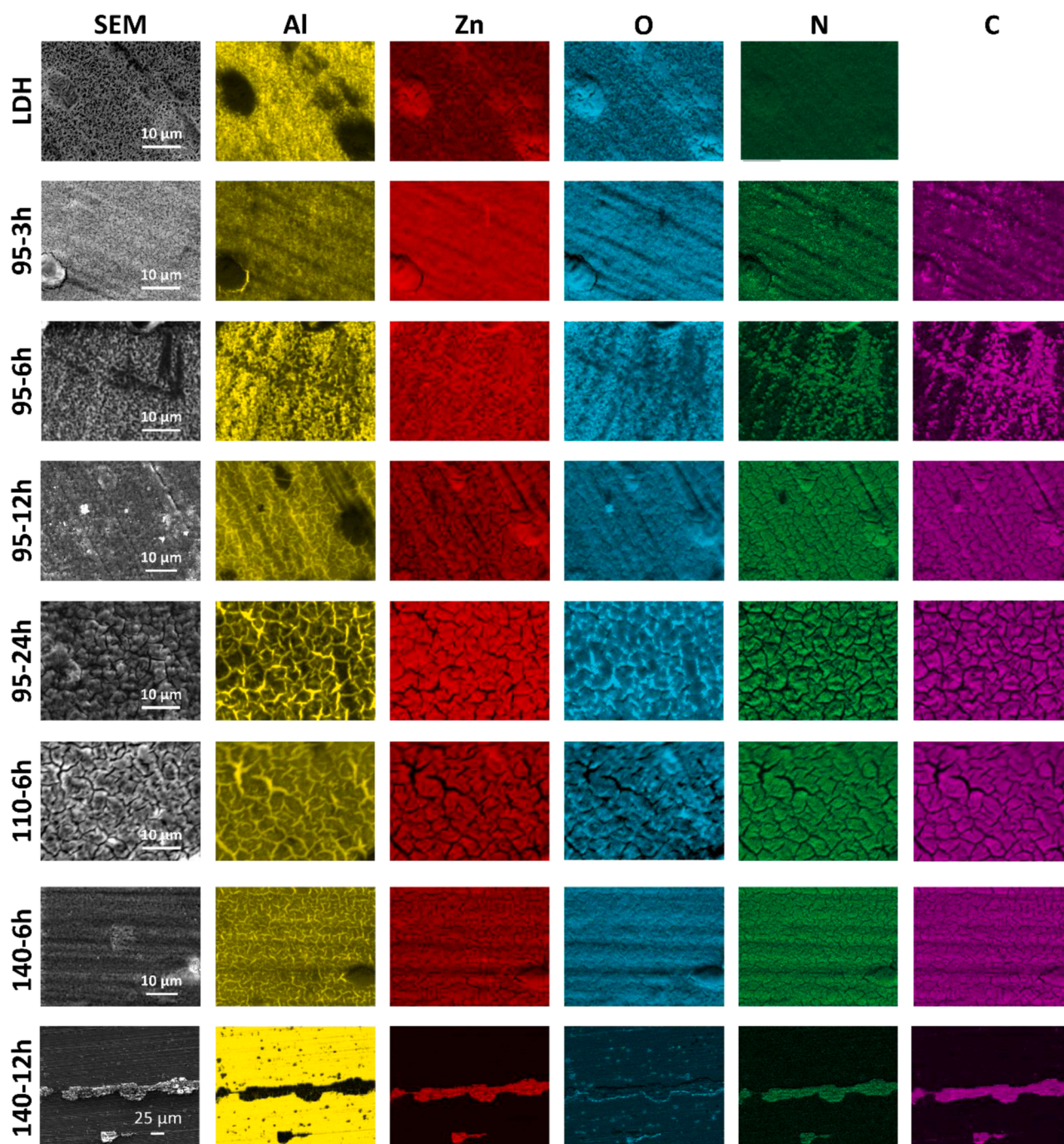
Fig. 6. EDS mapping of elemental distribution for initial Zn-Al LDH, 95-3h, 95-6h, 95-12h, 94-24h, 110-6h, 140-6h, 140-12h.

|Z| at 0.01 Hz for all specimens changed with time. Application of the LDH and ZIF-8@LDH coatings to AA2024 improved its corrosion resistance for almost all specimens (after 1 and 24 h of immersion). The maximum |Z| at 0.01 Hz was demonstrated by Zn-Al LDH coating after 1 h of exposure. However, the value dropped after 24 and 168 h and was than lower or comparable to one for the ZIF-8@LDH specimens. Conditions of the LDH-to-ZIF-8 recrystallisation affected its protective ability. Among the specimens from 95-t batch, the highest protection was provided by 95-12h, that demonstrated effective protection during the whole immersion period. Even more, this coating provided high level of corrosion protection even after 360 h of immersion into 0.5 wt.% NaCl solution (as it can be followed from Fig. SI6) that was comparable to the data for MOF-based coatings reported previously (Table SI3). This result also correlates with the results of SEM demonstrating the

formation of ZIF-8@LDH coating with a homogenous covering of the surface with ZIF-8 crystals and a lower amount of the surface defects (intercrystalline pores or cracks) comparing to 95-6h and 95-24h. Similarly, 110-6h and 140-6h demonstrated less effective corrosion protection due to inhomogeneous coverage with ZIF-8 crystals and the presence of cracks on the surface.

The EIS spectra for all specimens show the presence of several relaxation processes. However, the identification of all time constants was problematic due to their strong overlapping. To simplify the identification, the distribution of relaxation times (DRT) analysis was performed, whose results are presented in Fig. SI4. Based on the DRT analysis, the spectrum of uncoated AA2024 substrate after 1 h of immersion in 0.5 wt.% NaCl solution was characterised by two relaxation processes. The first one located at approximately 10 Hz was attributed to
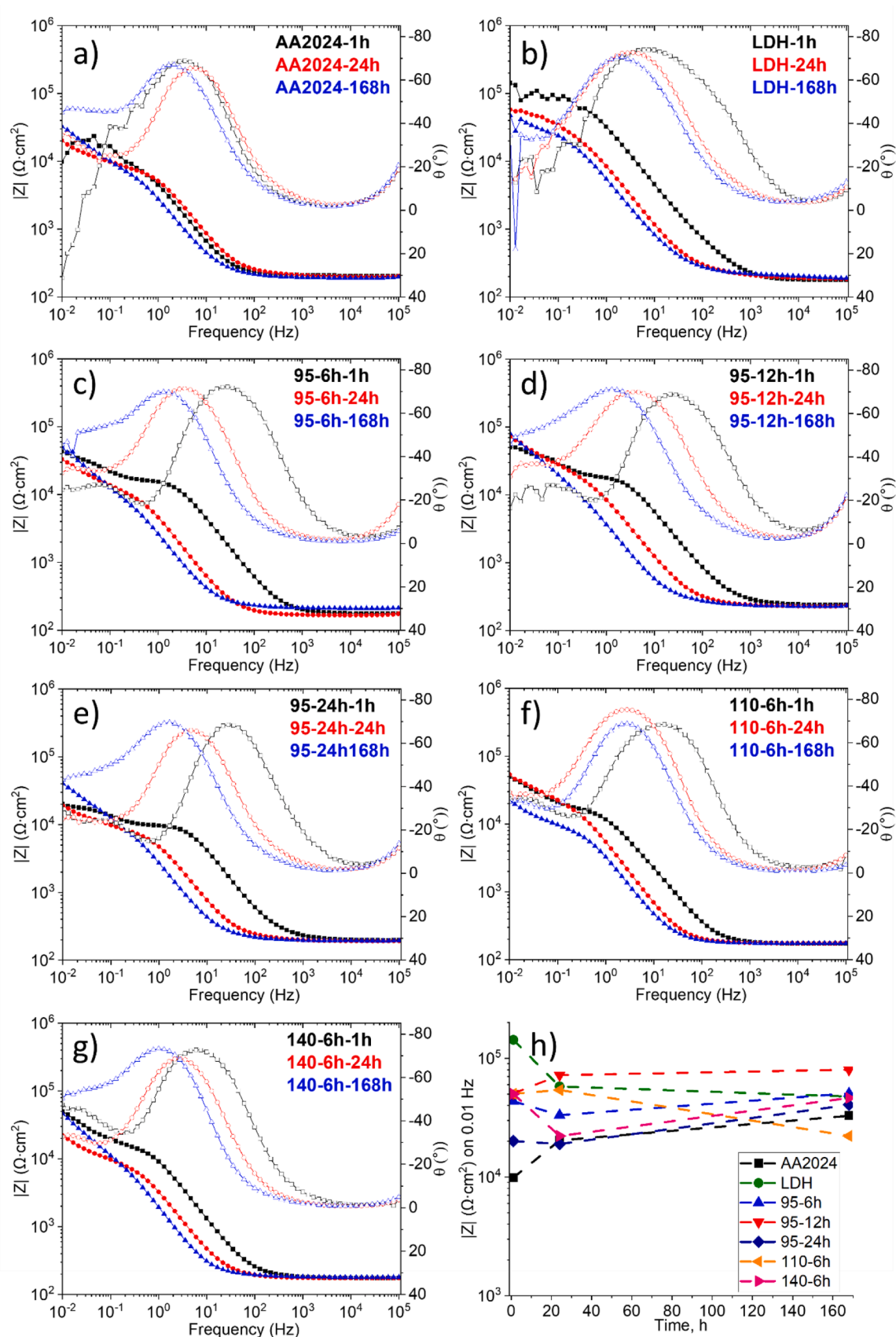
Fig. 7. Bode and phase angle plots for (a) bare AA2024 aluminium alloy and coated with (b) Zn-Al LDH; c) 95-6h, d) 95-12h, e) 95-24h, f) 110-6h, g) 140-6h after 1 h, 24 h and 168 h of immersion into 0.5 wt.% NaCl solution at 25 °C. g) Evolution of |Z| (Ω cm²) at 0.01 Hz with time for the specimens.

the presence of native aluminium oxide on the surface of aluminium alloy. The second one, in the region of around 1 Hz is most likely related to the electrochemical activities on the surface of alloy. Further prolongation of EIS analysis to 24 and 168 h resulted in the shift of the first constant to regions of lower frequencies (6 and 2 Hz, respectively), which was due to the destabilisation of the native oxide layer in the process of corrosion. Besides, the third relaxation constant around 0.02 Hz appears in both spectra, which is probably related to diffusion through the corrosion products to the metallic surface.

The spectrum of AA2024 alloy coated with Zn-Al LDH demonstrated the presence of three time constants at around 0.01, 1 and 10 Hz after 1 h of the immersion. While the first two constants are connected to the

charge transfer and response of oxide layer, the time constant at 10 Hz is originated from the weak response of LDH layer. However, as previously shown, the single LDH layer, which was not additionally intercalated with corrosion inhibitors, does not provide long-term protective effect [62,63]. And no evidence of the presence of this layer was observed after 24 and 168 h of the immersion.

Three relaxation processes were also identified for the spectra of all ZIF-8@LDH coatings after 1–168 h of immersion. After 1 h of immersion in 0.5 wt.% NaCl solution, the presence of the time constant in the region of 10–100 Hz was characteristic for all specimens, which was associated with a response of the ZIF-8@LDH coating together with oxide layer. This constant further moved to the regions of around 1 Hz after 24 and
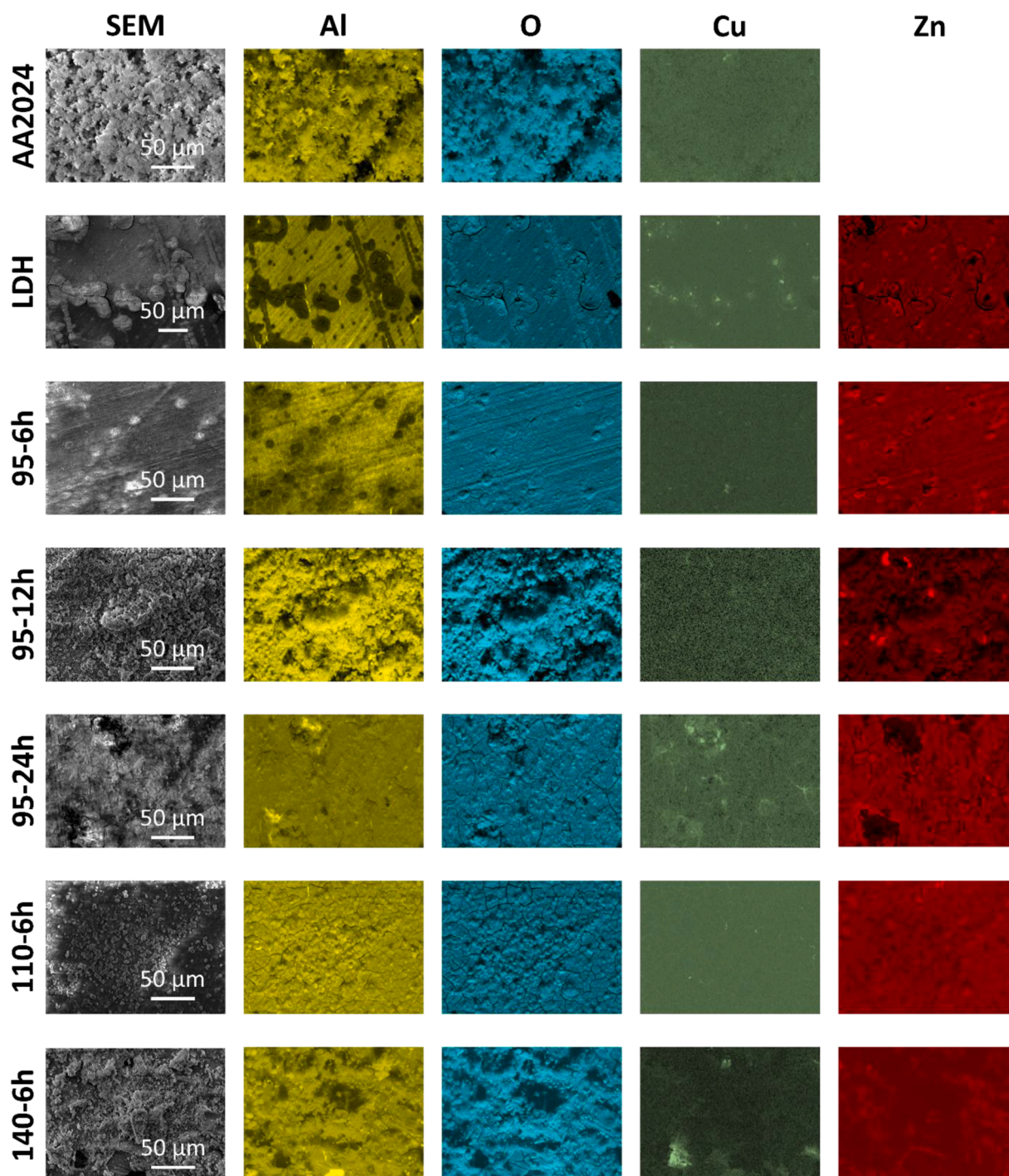

Fig. 8. SEM and EDS mappings of the bare AA2024 and coated with Zn-Al LDH, 95-6h, 95-12h, 95-24h, 110-6h, 140-6h after 168 h of EIS in 0.5 wt.% NaCl solution.

168 h of EIS, which was related to the partial decomposition of both layers in the process of corrosion. The time constant located at 0.1–1 Hz was most likely associated with corrosion processes on the surface. The third constant was in the range of 0.01–0.1 Hz based on the DRT analysis. And while for the beginning of the treatment, the process of charge transfer was responsible for its presence, diffusion through the porous product of corrosion contributed for this constant after the immersion for 24 and 168 h.

To obtain quantitative information about the corrosion performance of the bare AA2024 alloy, Zn-Al LDH and ZIF-8@Zn-Al LDH coatings, the EIS spectra were fitted. The equivalent circuits (ECs) used for the fitting were chosen in accordance with the DRT results. The ECs as well as an example of fitting are presented in the supporting information (Fig. SI5). Table SI2 provides numeric values obtained after the fitting. The EC (Fig. SI5, b)) was used to fit the spectra of AA2024 coated with Zn-Al LDH after 168 h, 95-6h, 95-12h, 110-6h, after 24 and 168 h, 95-24h and 140-6h after 1, 24 and 168 h of the immersion into the solution of 0.5 wt.% NaCl. This EC includes R_s, R_{ox} and CPE_{ox}, R_{ct} and CPE_{dl}, and W_s, which correspond to the solution resistance, the resistance and capacitance of the natural oxide layer, the charge transfer resistance and the double layer capacitance of the electrolyte/metal interface, and the porous Warburg impedance element, respectively. The spectra for the bare AA2024 alloy after 1 h, 24 h and 168 h of EIS testing were fitted using the EC (Fig. SI5, c), where R_s corresponds to the solution resistance, R_{ox} and CPE_{ox} to the resistance and capacitance of the natural oxide layer and R_{ct} and CPE_{dl}, to the resistance of charge transfer and the double layer capacitance. For fitting of the spectra of 95-6h, 95-12h and 110-6h after 1 h of the immersion, the EC (Fig. SI5, d)) was applied. It includes the solution resistance R_s, the resistance of charge transfer R_{ct} and the capacitance of double layer, CPE_{dl}, the resistance of natural oxide R_{ox} and its capacitance CPE_{ox}, the resistance of coating layer, R_{cot} and its capacitance CPE_{cot}. The EIS experimental data were fitted with chi-squared values in the range of 10^{-3}–10^{-1}.

Additionally, the protective ability of Zn-Al LDH and 95-12h coatings were compared by potentiodynamic polarization (Fig. SI7). In case of Zn-Al LDH coating slightly lower cathodic activity was observed, while for 95-12h, passivation of the surface was detected. Meanwhile, in general both coatings demonstrated comparable behaviour in potentiodynamic polarization test.

To get additional information about the corrosion process, the samples after 168 h of EIS testing were characterised by SEM and EDS (Fig. 8). Moreover, the elemental composition (average, wt.%) of the corrosion products after the immersion is presented in Table SI4, while compositions (wt.%) in the different points are shown in Fig. SI8. The specimen of uncoated AA2024 alloy was covered by extensive corrosion products, which were mainly composed of Al and O elements based on the EDS analysis (Table SI4, Fig. SI8). The specimen coated with Zn-Al LDH was covered by a lower amount of corrosion products also made of mainly Al and O, but pitting corrosion and cracks on the surface were detected. Both were located close to the Cu-rich intermetallics based on EDS analysis, which correlates with numerous investigations on the corrosion mechanism of AA2024 alloy demonstrating that in the case of this alloy, corrosion starts mainly near Cu-enriched intermetallis particles [64–68]. The EDS analyses also showed that the areas close to intermetallics were depleted with Al (Fig. SI8, 39.2 ± 1.1 % Al, 39.0 ± 1.1 % O, 10.2 ± 0.8 Cu). Moreover, based on the data of EDS analysis of the surface (Table SI4), this specimen was characterised by the highest concentration of Zn after immersion into to 0.5 wt.% NaCl solution. The surface of 95-6h looked similarly to parental Zn-Al LDH, but there have already been significantly less corrosion pits and cracks, whose size was smaller. It was also found that based on the EDS, the amount of Zn on the surface was significantly lower comparing to Zn-Al LDH samples. The 95-12h, 95-24h, 110-6h and 140-6h specimens were covered by higher amount of solid products comparing to Zn-Al LDH and 95-6h, but almost no corrosion pits were seen, except for 95-24h. Moreover, no surface cracks were visible for 95-12h, which generally correlates with EIS

results providing the highest level of corrosion protection. In all cases, mappings showed that Al and O were homogenously distributed. However, the surface and point elemental composition varied for all specimens demonstrating the values of Al and O in the range of 29.0–64.0 % and 29–62 %, respectively.

Additionally, in order to compare the composition of corrosion products formed on the surfaces, bare AA2024, Zn-Al LDH and 95-12h specimens were immersed into 0.5 wt.% NaCl solution at 25 °C for 168 h. Fig. 9 represents the XRD patterns and Raman spectra after the immersion. The XRD patterns (Fig. 9a) show that the crystalline products of corrosion were $Al(OH)_3$ (bayerite) phase (reflections at 18.3 and 20.2° 2θ) and Al_2O_3 (reflections at 15.9, 19.1 and 22.6° 2θ) for all specimens. Moreover, the LDH reflections were still presented in the XRD patterns of Zn-Al LDH and 95-12h. However, in the case of Zn-Al LDH, the (003) LDH reflection was shifted to 11.4 2θ°, which corresponds to the LDH structure intercalated with Cl^-. In the case of the 95-12h, the intensities of the LDH peaks were decreased, and their position was also slightly shifted into the region of high angles, which can indicate the started release of 2-mIm$^-$ and intercalation of Cl^- ions into the LDH gallery from the media. The Raman spectrum of bare AA2024 alloy was characterised by the presence of signals at 491 and 347 cm^{-1}, that correspond to AlOOH (boehmite) phase [69,70]. The Raman spectra of the corroded 95-12h and LDH specimens demonstrate the presence of an intensive signal at 559 cm^{-1}, which most likely corresponds to γ(OH) vibrations from $Al(OH)_3$ bayerite. Additionally to that, Al-O vibrations of bayerite were detected at 437, 385 and 323 cm^{-1} [69]. Moreover, the presence of the bands at 295 and 235 cm^{-1} in the spectrum of 95-12h, that could correspond to Cu-N vibration [71,72], confirm the release of 2-HmIm from ZIF-8 and/or LDH and its further adsorption on the Cu-rich intermetallics.

3.6. Discussion

In the frame of the current work, the treatment of Zn-Al LDH grown on the surface of AA2024 with 2-HmIm organic linkers in methanol was in the focus. The first part of the investigation aimed to understand the processes that take place during the treatment. *In situ* synchrotron (Fig. 3) and ex situ laboratory XRD (Fig. 2) analyses demonstrated that two parallel processes run on the surface: recrystallisation of Zn-Al LDH into ZIF-8 structure and intercalation of 2-mIm$^-$ into the LDH gallery (Fig. 10). It can be proposed that at the first stage of the treatment partial dissolution of LDH flakes located on the upper coating surface takes place (Eq. (1)):

$$Zn_2Al(OH)_6NO_3 \cdot 1.9H_2O \rightarrow 2\,Zn^{2+} + Al^{3+} + 6\,OH^- + NO_3^- + 1.9\,H_2O \quad (1)$$
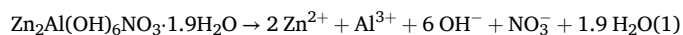
The process leads to the release of Zn^{2+}, Al^{3+}, OH^-, NO_3^- and H_2O to the methanol solution. Similar partial dissolution processes have been previously reported for LDH structures [74,75]. Due to the basic pH level of the methanolic solution of 2-HmIm [76] and elevated treatment temperatures, similar processes are expected also under the treatment conditions. These ions can further take part in the reconstruction of the LDH structure (Fig. 10, upper way), which is accompanied by the intercalation of 2-mIm$^-$ (Eq. (2)):

$$Zn^{2+} + Al^{3+} + OH^- + 2\text{-mIm}^- \rightarrow \text{Zn-Al LDH-2-mIm}^- \quad (2)$$
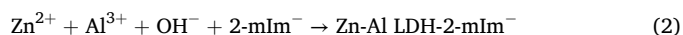
In turn, 2-mIm$^-$ anions are formed due to the deprotonation of 2-HmIm by OH^- released from LDH. In parallel, Zn^{2+} ions react with 2-mIm$^-$ organic linkers (Fig. 10, bottom way), that are present in the reaction mixture in surplus, forming ZIF-8 (Eq. 3):

$$Zn^{2+} + 2\,2\text{-mIm}^- \rightarrow Zn(2\text{-mIm})_2 \ (\textbf{ZIF-8}) \quad (3)$$
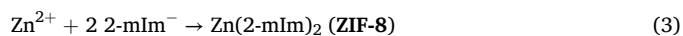
As it was demonstrated by the *in situ* synchrotron measurements, the intensities of the (110) and (200) ZIF-8 reflections as well as the (003) LDH reflection, vary with time. However, there were no main trends in their behaviour, i.e. their rising was followed by decreasing and back.
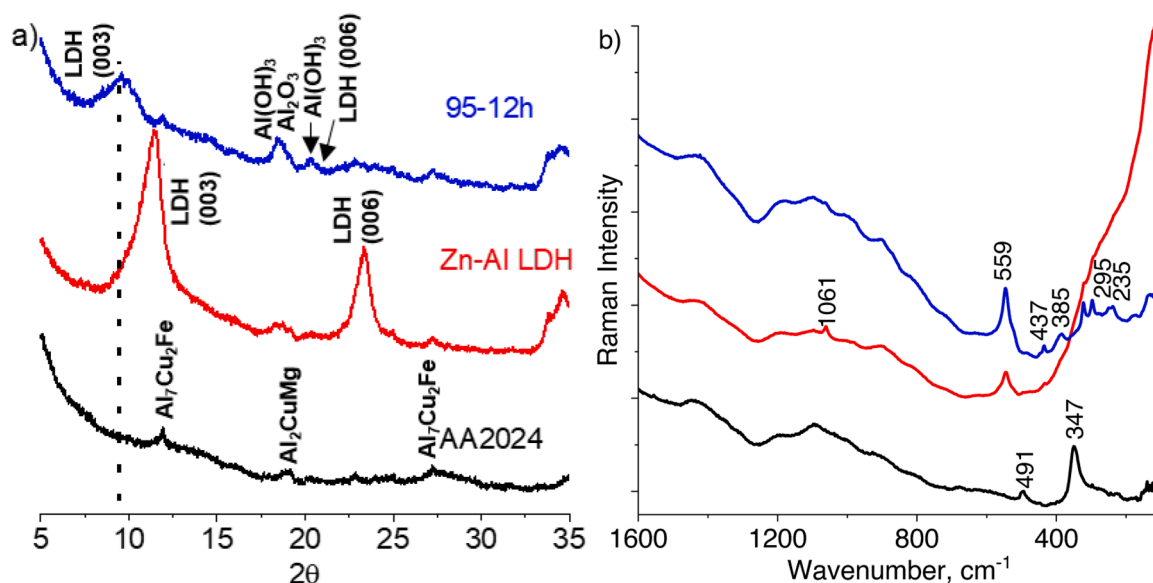
Fig. 9. a) XRD patterns and b) Raman spectra of bare AA2024, Zn-Al LDH and 95-12h after the immersion into 0.5 wt.% NaCl solution at 25 °C for 168 h. Al$_7$Cu$_2$Fe and Al$_2$CuMg are originated from AA2024 substrate. The band at 1061 cm^{-1} is attribute to contamination of LDH-CO$_3$ [2–73].
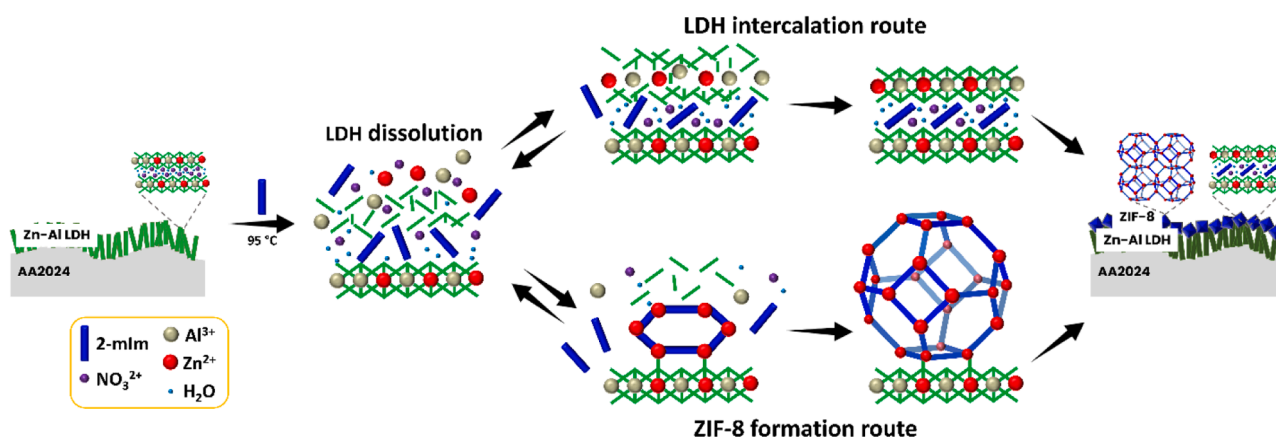

Fig. 10. Schematic representation of the processes taking place on the surface of AA2024 alloy covered with Zn-Al LDH after the treatment with methanolic solution of 2-HmIm.

And if, in the case of ZIF-8 crystals, it could be associated with crystals growth and their further detachment from the coating surface into the treatment bath, for the LDH flakes, such behaviour can indicate the reversibility of NO$_3^-$-to-2-mIm$^-$ intercalation process and consequently, formation of mixed LDH phase intercalated by both anions. Such an assumption also correlates with a variation of the d-spacings values with time. However, it should also be noted that the full NO$_3^-$-to-2-mIm$^-$ ion exchange is not possible under the reaction conditions, due to the participation of 2-HmIm in the ZIF-8 crystallisation parallelly running. Moreover, the ZIF-8 layer formed on the upper surface of the coating blocks the access of 2-HmIm to the deeper LDH flakes. In the case of ZIF-8, also a limitation in the crystallisation was observed by SEM (95-24h, Fig. 8e)). Thus, the continuous growth of ZIF-8 crystals on the surface in all directions led to the appearance of stresses in the layer, and, consequently, the formation of cracks and defects.

The treatment discussed previously resulted in the formation of the complex coating, which was composed of ZIF-8 and Zn-Al LDH intercalated with 2-mIm$^-$. This ZIF-8@Zn-Al LDH coating can provide effective corrosion protection by different ways. Firstly, such complex structure of the coating is beneficial, as both ZIF-8 and Zn-Al LDH belong to the nanocontainer compounds, i.e. both start to release 2-HmIm

corrosion inhibitor in corrosive media. Moreover, the obtained coating contains a higher amount of inhibitive 2-HmIm species and can provide extended protection. 2-HmIm belongs to the inhibitors from the azole group whose protective mechanism is based on adsorption on the surface, suppressing the dealloying of the intermetallic particles and decreasing oxygen reduction by blocking the copper-rich intermetallic phases [77–79]. ZIF-8 releases 2-HmIm upon structure decomposition. 2-mIm$^-$ intercalated into the LDH is ion-exchanged by Cl$^-$. Consequently, intercalation of Cl$^-$ anions into the LDH further postpones their transport to the metallic interface. Moreover, as it was shown by SEM, the crystallisation of ZIF-8 on the surface improves the barrier properties of the coating due to the covering of the inherent cavities and intercrystalline pores of the parental LDH film. However, EIS tests demonstrated that conditions of ZIF-8@Zn-Al LDH formation, including treatment temperature and time, affected the final coatings performance. Prolongation of the treatment time from 6 to 12 h at 95 °C was beneficial for protective properties of ZIF-8@Zn-Al LDH coatings. It was associated with the effective sealing of intercrystalline LDH pores/defects by ZIF-8 crystals and consequently formation of a denser coating on the surface. Even more, SEM micrographs of specimens treated for 3 and 6 h exhibited the presence of cracks in coatings close to

the "flower-like" LDH area located near intermetallics. In turn, their presence adversely affects on the corrosion protection, as they provide easy access for aggressive chloride ions to the Cu-rich intermetallic particles and can even accelerate the metal degradation. Thus, as it can be seen from Fig. 7h), 95-6h was less protective compared to the parental Zn-Al LDH coating. In turn, elevated temperatures, i.e. 110 and 140 °C, as well as increased treatment time, 24 h for 95 °C also negatively impacted the protective ability of the coating, as they resulted in the formation of inhomogeneous coatings or cracks on the surface also facilitating the transport of aggressive anions to the metallic interface. Summarising all the data discussed previously, it can be concluded, that the protective ability of Zn-Al LDH coating can be further adjected by post-modification with ZIF-8 but only under control of the treatment conditions of the process. Finally, it should also be pointed out, that investigation of the kinetics of ZIF-8 dissolution from the surface is still required to clarify the mechanism of corrosion protection of AA2024 alloy.

4. Conclusions

Formation of ZIF-8@Zn-Al LDH from Zn-Al LDH conversion coating on the surface of AA2024 aluminium alloy was in the focus of the current investigation. Zn-Al LDH was partially recrystallised into ZIF-8 structure in methanolic solution of 2-HmIm after the treatment at 95–110 °C for 3–24 h. Moreover, the process was accompanied by partial NO_3^- to 2-mIm$^-$ ion exchange inside the LDH gallery. Conditions of the ZIF-8@Zn-Al LDH preparation (temperature and time) affected the final protective ability of the coatings based on EIS results. The highest corrosion resistance was provided by the coating obtained at 95 °C for 12 h. It was associated with nanocontainer properties of both ZIF-8 and Zn-Al LDH and consequent loading of a higher amount of 2-HmIm inhibitors as well as with covering of the inherent cavities and intercrystalline pores of the initial LDH with ZIF-8 crystals resulting in enhanced barrier properties of the coating.

CRediT authorship contribution statement

Valeryia Kasneryk: Writing – review & editing, Writing – original draft, Visualization, Project administration, Investigation, Formal analysis, Data curation, Conceptualization. **Eugen Gazenbiller:** Writing – review & editing, Investigation. **D.C. Florian Wieland:** Writing – review & editing, Software, Investigation, Data curation. **Vasil M. Garamus:** Writing – review & editing, Investigation. **Maria Serdechnova:** Writing – review & editing, Investigation. **Carsten Blawert:** Writing – review & editing, Supervision, Investigation. **Mikhail L. Zheludkevich:** Writing – review & editing, Supervision.

Declaration of competing interest

The authors declare the following financial interests/personal relationships which may be considered as potential competing interests:

Valeryia Kasneryk reports financial support was provided by Alexander von Humboldt Foundation. If there are other authors, they declare that they have no known competing financial interests or personal relationships that could have appeared to influence the work reported in this paper.

Acknowledgements

Supplementary materials

Supplementary material associated with this article can be found, in the online version, at doi:10.1016/j.surfin.2025.105958.

Data availability

Data will be made available on request.

References

[1] R.C. Dorward, T.R. Pritchett, Advanced aluminium alloys for aircraft and aerospace applications, Mater. Des. 9 (2) (1988) 63–69, https://doi.org/10.1016/0261-3069 (88)90076-3.

[2] M.A. Wahid, A.N. Siddiquee, Z.A. Khan, Aluminum alloys in marine construction: characteristics, application, and problems from a fabrication viewpoint, Mar. Syst. Ocean Technol. 15 (1) (2020) 70–80, https://doi.org/10.1007/s40868-019-00069-w.

[3] W.S. Miller, L. Zhuang, J. Bottema, A.J. Wittebrood, P. De Smet, A. Haszler, A. Vieregge, Recent development in aluminium alloys for the automotive industry, Mater. Sci. Eng. 280 (1) (2000) 37–49, https://doi.org/10.1016/S0921-5093(99)00653-X.

[4] D. Varshney, K. Kumar, Application and use of different aluminium alloys with respect to workability, strength and welding parameter optimization, Ain Shams Eng. J. 12 (1) (2021) 1143–1152, https://doi.org/10.1016/j.asej.2020.05.013.

[5] H. Zhu, J. Li, Advancements in corrosion protection for aerospace aluminum alloys through surface treatment, Int. J. Electrochem. Sci. 19 (2) (2024) 100487, https://doi.org/10.1016/j.ijoes.2024.100487.

[6] A. Emre, R. Shashanka, M. Vutukuru, Introductory chapter: introduction to aluminum alloys, in: R. Shashanka (Ed.), Recent Advancements in Aluminum Alloys, IntechOpen, Rijeka, 2024 p Ch. 1.

[7] L. Jiang, Y. Dong, Y. Yuan, X. Zhou, Y. Liu, X. Meng, Recent advances of metal–organic frameworks in corrosion protection: from synthesis to applications, Chem. Eng. J. 430 (2022) 132823, https://doi.org/10.1016/j.cej.2021.132823.

[8] P. Rani, V. Kasneryk, M. Opanasenko, MOF-inorganic nanocomposites: bridging a gap with inorganic materials, Appl. Mater. Today 26 (2022) 101283, https://doi.org/10.1016/j.apmt.2021.101283.

[9] N. Stock, S. Biswas, Synthesis of metal-organic frameworks (MOFs): routes to various MOF topologies, morphologies, and composites, Chem. Rev. 112 (2) (2012) 933–969, https://doi.org/10.1021/cr200304e.

[10] J. Zhang, Y. Tan, W.-J. Song, Zeolitic imidazolate frameworks for use in electrochemical and optical chemical sensing and biosensing: a review, Microchim. Acta 187 (4) (2020) 234, https://doi.org/10.1007/s00604-020-4173-3.

[11] M.Y. Zorainy, M. Sheashea, S. Kaliaguine, M. Gobara, D.C. Boffito, Facile solvothermal synthesis of a MIL-47(V) metal–organic framework for a high-performance epoxy/MOF coating with improved anticorrosion properties, RSC Adv. 12 (15) (2022) 9008–9022, https://doi.org/10.1039/D1RA08950A.

[12] M.F. Montemor, Functional and smart coatings for corrosion protection: a review of recent advances, Surf. Coat. Technol. 258 (2014) 17–37, https://doi.org/10.1016/j.surfcoat.2014.06.031.

[13] V. Kasneryk, M. Serdechnova, C. Blawert, M.L. Zheludkevich, LDH has been grown: what is next? Overview on methods of post-treatment of LDH conversion coatings, Appl. Clay Sci. 232 (2023) 106774, https://doi.org/10.1016/j.clay.2022.106774.

[14] M. Tabish, G. Yasin, M.J. Anjum, M.U. Malik, J.M. Zhao, Q.X. Yang, S. Manzoor, H. Murtaza, W.Q. Khan, Reviewing the current status of layered double hydroxide-based smart nanocontainers for corrosion inhibiting applications, J. Mater. Res. Technol. 10 (2021) 390–421, https://doi.org/10.1016/j.jmrt.2020.12.025.

[15] D.G. Shchukin, Container-based multifunctional self-healing polymer coatings, Polym. Chem. 4 (18) (2013) 4871–4877, https://doi.org/10.1039/C3PY00082F.

[16] Y. Zhang, P. Yu, J. Wu, F. Chen, Y. Li, Y. Zhang, Y. Zuo, Y. Qi, Enhancement of anticorrosion protection via inhibitor-loaded ZnAlCe-LDH nanocontainers embedded in sol–gel coatings, J. Coat. Technol. Res. 15 (2) (2018) 303–313, https://doi.org/10.1007/s11998-017-9978-6.

[17] K. Wei, Y. Wei, Y. Zhang, V. Kasneryk, M. Serdechnova, H. Wang, Z. Zhang, Y. Yuan, C. Blawert, M.L. Zheludkevich, F. Chen, In situ synthesis of ZIF-8 loaded with 8-hydroxyquinoline composite via a host-guest nanoconfinement strategy for high-performance corrosion protection, Corros. Sci. 227 (2024) 111731, https://doi.org/10.1016/j.corsci.2023.111731.

[18] Z. Mohammadpour, H.R. Zare, Fabrication of a pH-sensitive epoxy nanocomposite coating based on a Zn-BTC metal–Organic framework containing benzotriazole as a smart corrosion inhibitor, Cryst. Growth Des. 21 (7) (2021) 3954–3966, https://doi.org/10.1021/acs.cgd.1c00284.

[19] Y. Huang, C. Zhao, Y. Li, C. Wang, W. Yuan, T. Shen, J. Liu, D. Cheng, C. Wu, Q. Shen, H. Ding, S. Chen, H. Yang, A smart sol–gel coating incorporating pH-responsive BTA-ZIF-8 MOF assembled hexagonal boron nitride for active/passive corrosion protection of 1060 aluminum alloy, Surf. Coat. Technol. 474 (2023) 130072, https://doi.org/10.1016/j.surfcoat.2023.130072.

[20] W. Kong, M. Serdechnova, V. Kasneryk, D. Gao, H. Wang, X. Xie, C. Blawert, M.L. Zheludkevich, Y. Zhang, ZIF-8 based bifunctional coatings with anticorrosive and antibacterial properties: a new design strategy for more efficiency, Surf. Coat. Technol. 483 (2024) 130812, https://doi.org/10.1016/j.surfcoat.2024.130812.

[21] D. Fan, X. Liu, K. Qi, Z. Chen, Y. Qiu, B. Liao, X. Guo, A smart-sensing coating based on dual-emission fluorescent Zr-MOF composite for autonomous warning of

coating damage and aluminum corrosion, Prog. Org. Coat. 172 (2022) 107150, https://doi.org/10.1016/j.porgcoat.2022.107150.

[22] Y.J. Tarzanagh, D. Seifzadeh, Z. Rajabalizadeh, A. Habibi-Yangjeh, A. Khodayari, S. Sohrabnezhad, Sol–gel/MOF nanocomposite for effective protection of 2024 aluminum alloy against corrosion, Surf. Coat. Technol. 380 (2019) 125038, https://doi.org/10.1016/j.surfcoat.2019.125038.

[23] L. Xiong, J. Liu, M. Yu, S. Li, Improving the corrosion protection properties of PVB coating by using salicylaldehyde@ZIF-8/graphene oxide two-dimensional nanocomposites, Corros. Sci. 146 (2019) 70–79, https://doi.org/10.1016/j.corsci.2018.10.016.

[24] M. Zhang, L. Ma, L.L. Wan, Y.W. Sun, Y. Liu, Insights into the use of metal-organic framework as high-performance anticorrosion coatings, ACS Appl. Mater. Interfaces 10 (3) (2018) 2259–2263, https://doi.org/10.1021/acsami.7b18713.

[25] M. Zhang, Y. Liu, Enhancing the anti-corrosion performance of ZIF-8-based coatings via microstructural optimization, New J. Chem. 44 (7) (2020) 2941–2946, https://doi.org/10.1039/c9nj05998a.

[26] Z. Zhang, J. Wang, M. Serdechnova, V. Kasneryk, Z. Zhang, C. Blawert, H. Wang, M.L. Zheludkevich, F. Chen, Y. Zhang, An inhibitor-loaded LDH- and MOF-based bilayer hybrid system for active corrosion protection of aluminum alloys, ACS Appl. Mater. Interfaces 16 (9) (2024) 11944–11956, https://doi.org/10.1021/acsami.3c19432.

[27] Y. Liu, J.H. Pan, N.Y. Wang, F. Steinbach, X.L. Liu, J. Caro, Remarkably enhanced gas separation by partial self-conversion of a laminated membrane to metal-organic frameworks, Angew. Chem. - Int. Ed. 54 (10) (2015) 3028–3032, https://doi.org/10.1002/anie.201411550.

[28] Y. Liu, N.Y. Wang, J.H. Pan, F. Steinbach, J.In Caro, Situ synthesis of MOF membranes on ZnAl-CO$_3$ LDH buffer layer-modified substrates, J. Am. Chem. Soc. 136 (41) (2014) 14353–14356, https://doi.org/10.1021/ja0507408s.

[29] V. Kasneryk, T. Wu, H. Rohr, M. Serdechnova, K. Mojsilović, D.C.F. Wieland, A. Davydok, E. Gazenbiller, R. Vasilić, C. Blawert, N. Stock, M.L. Zheludkevich, Controllable recrystallization of ZnO/ZnAl$_2$O$_4$ based PEO into ZIF-8 as a route for the formation of multifunctional coatings, J. Ind. Eng. Chem. 132 (2024) 395–409, https://doi.org/10.1016/j.jiec.2023.11.033.

[30] V. Kasneryk, M.P.M. Poschmann, M. Serdechnova, G. Dovzhenko, D.C.F. Wieland, P. Karlova, T. Naacke, M. Starykevich, C. Blawert, N. Stock, M.L. Zheludkevich, Formation and structure of ZIF-8@PEO coating on the surface of zinc, Surf. Coat. Technol. 445 (2022) 128733, https://doi.org/10.1016/j.surfcoat.2022.128733.

[31] L. Telmenbayar, A. Gopal Ramu, D. Yang, D. Choi, Development of mechanically robust and anticorrosion slippery PEO coating with metal–organic framework (MOF) of magnesium alloy, Chem. Eng. J. 458 (2023) 141397, https://doi.org/10.1016/j.cej.2023.141397.

[32] Y. Chen, L. Wu, W. Yao, J. Wu, J. Xiang, X. Dai, T. Wu, Y. Yuan, J. Wang, B. Jiang, F. Pan, Development of metal-organic framework (MOF) decorated graphene oxide/MgAl-layered double hydroxide coating via microstructural optimization for anti-corrosion micro-arc oxidation coatings of magnesium alloy, J. Mater. Sci. Technol. 130 (2022) 12–26, https://doi.org/10.1016/j.jmst.2022.03.039.

[33] S. Jin, Z. Jie, R. Wu, X. Ma, Z. Yu, W. Guixiang, J. Zhang, B. Krit, S. Betsofen, N. Vitalii, B. Ruslan, M. Qiu, Y. Yang, J. Chen, In-situ growth of corrosion-resistant LDH/ZIF-8 hybrid film on the surface of MAO film based on LA93 alloy by the one-step method, Appl. Surf. Sci. 671 (2024) 160742, https://doi.org/10.1016/j.apsusc.2024.160742.

[34] K.S. Park, Z. Ni, A.P. Côté, J.Y. Choi, R. Huang, F.J. Uribe-Romo, H.K. Chae, M. O'Keeffe, O.M. Yaghi, Exceptional chemical and thermal stability of zeolitic imidazolate frameworks, Proc. Natl. Acad. Sci. 103 (27) (2006) 10186–10191, https://doi.org/10.1073/pnas.0602439103.

[35] H. Zhang, M. Zhao, Y.S. Lin, Stability of ZIF-8 in water under ambient conditions, Microporous Mesoporous Mater. 279 (2019) 201–210, https://doi.org/10.1016/j.micromeso.2018.12.035.

[36] N. Talukder, Y. Wang, B.B. Nunna, X. Tong, E.S. Lee, An investigation on the structural stability of ZIF-8 in water versus water-derived oxidative species in aqueous environment, Microporous Mesoporous Mater. 366 (2024) 112934, https://doi.org/10.1016/j.micromeso.2023.112934.

[37] A.C. Bouali, M.H. Iuzviuk, M. Serdechnova, K.A. Yasakau, D.C.F. Wieland, G. Dovzhenko, H. Maltanava, I.A. Zobkalo, M.G.S. Ferreira, M.L. Zheludkevich, Zn-Al LDH growth on AA2024 and zinc and their intercalation with chloride: comparison of crystal structure and kinetics, Appl. Surf. Sci. 501 (2020) 144027, https://doi.org/10.1016/j.apsusc.2019.144027.

[38] A.C. Bouali, M.H. Iuzviuk, M. Serdechnova, K.A. Yasakau, D. Drozdenko, A. Lutz, K. Fekete, G. Dovzhenko, D.C.F. Wieland, H. Terryn, M.G.S. Ferreira, I.A. Zobkalo, M.L. Zheludkevich, Mechanism of LDH direct growth on aluminum alloy surface: a kinetic and morphological approach, J. Phys. Chem. C 125 (21) (2021) 11687–11701, https://doi.org/10.1021/acs.jpcc.1c02281.

[39] G. Ashiotis, A. Deschildre, Z. Nawaz, J.P. Wright, D. Karkoulis, F.E. Picca, J. Kieffer, The fast azimuthal integration Python library: pyFAI, J. Appl. Crystallogr. 48 (2) (2015) 510–519, https://doi.org/10.1107/S1600576715004306.

[40] T.J. Collins, ImageJ for microscopy, Biotechniques 43 (sup1) (2007) S25–S30, https://doi.org/10.2144/000112517.

[41] S. Britto, A.V. Radha, N. Ravishankar, P.V. Kamath, Solution decomposition of the layered double hydroxide (LDH) of Zn with Al, Solid State Sci. 9 (3) (2007) 279–286, https://doi.org/10.1016/j.solidstatesciences.2007.01.002.

[42] M.V. Bukhtiyarova, A review on effect of synthesis conditions on the formation of layered double hydroxides, J. Solid State Chem. 269 (2019) 494–506, https://doi.org/10.1016/j.jssc.2018.10.018.

[43] X. Zhao, Y. Yuan, Y. Wei, Z. Zhang, Y. Zhang, LDH-based "smart" films for corrosion sensing and protection, Materials 16 (9) (2023) 3483, https://doi.org/10.3390/ma16093483.

[44] Y. Zhang, J.H. Liu, Y.D. Li, M. Yu, S.M. Li, B. Xue, Fabrication of inhibitor anion-intercalated layered double hydroxide host films on aluminum alloy 2024 and their anticorrosion properties, J. Coat. Technol. Res. 12 (2) (2015) 293–302, https://doi.org/10.1007/s11998-014-9644-1.

[45] L.D. Wang, Q.F. Zong, W. Sun, Z.Q. Yang, G.C. Liu, Chemical modification of hydrotalcite coating for enhanced corrosion resistance, Corros. Sci. 93 (2015) 256–266, https://doi.org/10.1016/j.corsci.2015.01.033.

[46] S. Miyata, Anion-exchange properties of hydrotalcite-like compounds, Clays Clay Miner. 31 (4) (1983) 305–311, https://doi.org/10.1346/ccmn.1983.0310409.

[47] M.H. Iuzviuk, A.C. Bouali, M. Serdechnova, K.A. Yasakau, D.C.F. Wieland, G. Dovzhenko, A. Mikhailau, C. Blawert, I.A. Zobkalo, M.G.S. Ferreira, M.L. Zheludkevich, In situ kinetics studies of Zn-Al LDH intercalation with corrosion related species, Phys. Chem. Chem. Phys 22 (31) (2020) 17574–17586, https://doi.org/10.1039/d0cp01765e.

[48] D. Wu, F. He, Y. Dai, Y. Xie, Y. Ling, L. Liu, J. Zhao, H. Ye, Y. Hou, A heterostructured ZnAl-LDH@ZIF-8 hybrid as a bifunctional photocatalyst/adsorbent for CO$_2$ reduction under visible light irradiation, Chem. Eng. J. 446 (2022) 137003, https://doi.org/10.1016/j.cej.2022.137003.

[49] M. Klimakow, J. Leiterer, J. Kneipp, E. Rössler, U. Panne, K. Rademann, F. Emmerling, Combined synchrotron XRD/raman measurements: in situ identification of polymorphic transitions during crystallization processes, Langmuir 26 (13) (2010) 11233–11237, https://doi.org/10.1021/la100540q.

[50] L.L. DeMatos, A.C. Williams, S.W. Booth, C.R. Petts, D.J. Taylor, N. Blagden, Solvent influences on metastable polymorph lifetimes: real-time interconversions using energy dispersive X-ray diffractometry, J. Pharm. Sci. 96 (5) (2007) 1069–1078, https://doi.org/10.1002/jps.20924.

[51] Z. Zhang, Z. Hua, J. Lang, Y. Song, Q. Zhang, Q. Han, H. Fan, M. Gao, X. Li, J. Yang, Eco-friendly nanostructured Zn–Al layered double hydroxide photocatalysts with enhanced photocatalytic activity, CrystEngComm 21 (31) (2019) 4607–4619, https://doi.org/10.1039/C9CE00530G.

[52] G. Kumari, K. Jayaramulu, T.K. Maji, C. Narayana, Temperature induced structural transformations and gas adsorption in the zeolitic imidazolate framework ZIF-8: a Raman study, J. Phys. Chem. A 117 (43) (2013) 11006–11012, https://doi.org/10.1021/jp407792a.

[53] D.A. Carter, J.E. Pemberton, Raman spectroscopy and vibrational assignments of 1- and 2-methylimidazole, J. Raman Spectrosc. 28 (12) (1997) 939–946, https://doi.org/10.1002/(SICI)1097-4555(199712)28:12<939::AID-JRS186>3.0.CO;2-R.

[54] J. Li, H. Chang, Y. Li, Q. Li, K. Shen, H. Yi, J. Zhang, Synthesis and adsorption performance of La@ZIF-8 composite metal–organic frameworks, RSC Adv. 10 (6) (2020) 3380–3390, https://doi.org/10.1039/C9RA10548D.

[55] M. Cavallo, M. Dosa, R. Nakazato, N.G. Porcaro, M. Signorile, M. Quintelier, J. Hadermann, S. Bordiga, N.C. Rosero-Navarro, K. Tadanaga, V. Crocellà, F. Bonino, Insight on Zn-Al LDH as electrocatalyst for CO$_2$ reduction reaction: an in-situ ATR-IR study, J. CO$_2$ Util. 83 (2024) 102804, https://doi.org/10.1016/j.jcou.2024.102804.

[56] Z. Karami, Z. Jouyandeh, J.A. Ali, M.R. Ganjali, M. Aghazadeh, S.M.R. Paran, G. Naderi, D. Puglia, M.R. Saeb, Epoxy/layered double hydroxide (LDH) nanocomposites: synthesis, characterization, and excellent cure feature of nitrate anion intercalated Zn-Al LDH, Prog. Org. Coat. 136 (2019) 105218, https://doi.org/10.1016/j.porgcoat.2019.105218.

[57] J.-H. Liu, Y.-H. Zhang, L.-Y. Wang, Z.-F. Wei, Drawing out the structural information of the first layer of hydrated ions: ATR-FTIR spectroscopic studies on aqueous NH$_4$NO$_3$, NaNO$_3$, and Mg(NO$_3$)$_2$ solutions, Spectrochim. Acta Part A 61 (5) (2005) 893–899, https://doi.org/10.1016/j.saa.2004.06.030.

[58] S. Bhattacharyya, S.H. Pang, M.R. Dutzer, R.P. Lively, K.S. Walton, D.S. Sholl, S. Nair, Interactions of SO$_2$-containing acid gases with ZIF-8: structural changes and mechanistic investigations, J. Phys. Chem. C 120 (48) (2016) 27221–27229, https://doi.org/10.1021/acs.jpcc.6b09197.

[59] S. He, L. Wu, X. Li, H. Sun, T. Xiong, J. Liu, C. Huang, H. Xu, H. Sun, W. Chen, R. Gref, J. Zhang, Metal-organic frameworks for advanced drug delivery, Acta Pharm. Sin. B 11 (8) (2021) 2362–2395, https://doi.org/10.1016/j.apsb.2021.03.019.

[60] J. Tedim, M.L. Zheludkevich, A.C. Bastos, A.N. Salak, A.D. Lisenkov, M.G.S. Ferreira, Influence of preparation conditions of layered double hydroxide conversion films on corrosion protection, Electrochim. Acta 117 (2014) 164–171, https://doi.org/10.1016/j.electacta.2013.11.111.

[61] A.C. Bouali, M. Serdechnova, K.A. Yasakau, A. Lutz, G. Wiese, H. Terryn, M.G.S. Ferreira, M.L. Zheludkevich, The role of Cu-based intermetallic on the direct growth of a ZnAl LDH film on AA2024, J. Electrochem. Soc. 169 (8) (2022) 081501, https://doi.org/10.1149/1945-7111/ac83f5.

[62] J. Stephan, V. Kasneryk, M. Serdechnova, N. Scharnagl, E. Gazenbiller, B. Vaghefinazari, P. Volovitch, M. Starykevich, C. Blawert, M.L. Zheludkevich, Formation of Li-Al LDH conversion layer on AA2024 alloy for corrosion protection, Appl. Surf. Sci. 659 (2024) 159919, https://doi.org/10.1016/j.apsusc.2024.159919.

[63] Shulha, T.; Serdechnova, M.; Lamaka, S.V.; Lu, X.; Feiler, C.; Blawert, C.; Zheludkevich, M.L. Corrosion inhibitors intercalated into layered double hydroxides prepared In situ on AZ91 magnesium alloys: structure and protection ability. *ACS Appl. Mater. Interfaces* 2023, 15 (4), 6098–6112, DOI: 10.1021/acsami.2c18675.

[64] G. Williams, A.J. Coleman, H.N. McMurray, Inhibition of aluminium alloy AA2024-T3 pitting corrosion by copper complexing compounds, Electrochim. Acta 55 (20) (2010) 5947–5958, https://doi.org/10.1016/j.electacta.2010.05.049.

[65] R.G. Buchheit, M.A. Martinez, L.P. Montes, Evidence for Cu ion formation by dissolution and dealloying the Al2CuMg intermetallic compound in rotating ring-disk collection experiments, J. Electrochem. Soc. 147 (1) (2000) 119, https://doi.org/10.1149/1.1393164.

[66] W. Qafsaoui, M.W. Kendig, H. Perrot, H. Takenouti, Effect of 1-pyrrolidine dithiocarbamate on the galvanic coupling resistance of intermetallics—Aluminum matrix during corrosion of AA 2024-T3 in a dilute NaCl, Corros. Sci. 92 (2015) 245–255, https://doi.org/10.1016/j.corsci.2014.12.011.

[67] N. Birbilis, R.G. Buchheit, Electrochemical characteristics of intermetallic phases in aluminum alloys: an experimental survey and discussion, J. Electrochem. Soc. 152 (4) (2005) B140, https://doi.org/10.1149/1.1869984.

[68] K.A. Yasakau, M.L. Zheludkevich, S.V. Lamaka, M.G.S. Ferreira, Mechanism of corrosion inhibition of AA2024 by rare-earth compounds, J. Phys. Chem. B 110 (11) (2006) 5515–5528, https://doi.org/10.1021/jp0560664.

[69] A. Lekatou, A.K. Sfikas, A.E. Karantzalis, D. Sioulas, Microstructure and corrosion performance of Al-32 %Co alloys, Corros. Sci. 63 (2012) 193–209, https://doi.org/10.1016/j.corsci.2012.06.002.

[70] A. Kreta, M. Rodošek, L. Slemenik Perše, B. Orel, M. Gaberšček, A. Šurca Vuk, In situ electrochemical AFM, ex situ IR reflection–absorption and confocal Raman studies of corrosion processes of AA 2024-T3, Corros. Sci. 104 (2016) 290–309, https://doi.org/10.1016/j.corsci.2015.12.023.

[71] P. Naumov, O. Grupče, G. Jovanovski, Experimental and theoretical Raman study of the binuclear copper(II) imidazole saccharinato complex, J. Raman Spectrosc. 31 (6) (2000) 475–479, https://doi.org/10.1002/1097-4555(200006)31:6<475::AID-JRS559>3.0.CO;2-0.

[72] E.F. Silva, M.C.E. Bandeira, W.A. Alves, O.R. Mattos, Surface-enhanced Raman scattering and electrochemical investigations on the adsorption of imidazole: imidazolium couple and its implications on copper corrosion inhibition, J. Electrochem. Soc. 165 (7) (2018) C375, https://doi.org/10.1149/2.0841807jes.

[73] J.T. Kloprogge, D. Wharton, L. Hickey, R.L. Frost, Infrared and Raman study of interlayer anions CO_3^{2-}, NO_3^-, SO_4^{2-} and ClO_4^- in Mg/Al-hydrotalcite, Am. Mineral. 87 (5-6) (2002) 623–629, https://doi.org/10.2138/am-2002-5-604.

[74] H. Liu, Y. Wang, X. Lu, Y. Hu, G. Zhu, R. Chen, L. Ma, L. Zhu, Z. Tie, J. Liu, Z. Jin, The effects of Al substitution and partial dissolution on ultrathin NiFeAl trinary layered double hydroxide nanosheets for oxygen evolution reaction in alkaline solution, Nano Energy 35 (2017) 350–357, https://doi.org/10.1016/j.nanoen.2017.04.011.

[75] T. Shulha, M. Serdechnova, T. Wu, T. Naacke, G. Wiese, C. Blawert, M. L. Zheludkevich, LDH sealing for PEO coated friction stir welded AZ31/AA5754 materials, Nano Mater. Sci. 6 (2024) 428–442, https://doi.org/10.1016/j.nanoms.2024.02.009.

[76] Y. Li, C. Ma, P. Nian, H. Liu, X. Zhang, Green synthesis of ZIF-8 tubular membranes from a recyclable 2-methylimidazole water-solvent solution by ZnO nanorods self-converted strategy for gas separation, J. Memb. Sci. 581 (2019) 344–354, https://doi.org/10.1016/j.memsci.2019.03.069.

[77] A. Mishra, J. Aslam, C. Verma, M.A. Quraishi, E.E. Ebenso, Imidazoles as highly effective heterocyclic corrosion inhibitors for metals and alloys in aqueous electrolytes: a review, J. Taiwan Inst. Chem. Eng. 114 (2020) 341–358, https://doi.org/10.1016/j.jtice.2020.08.034.

[78] M.L. Zheludkevich, K.A. Yasakau, S.K. Poznyak, M.G.S. Ferreira, Triazole and thiazole derivatives as corrosion inhibitors for AA2024 aluminium alloy, Corros. Sci. 47 (12) (2005) 3368–3383, https://doi.org/10.1016/j.corsci.2005.05.040.

[79] E. Ech-chihbi, R. Salim, M. Ouakki, M. Koudad, L. Guo, M. Azam, N. Benchat, Z. Rais, M. Taleb, Corrosion resistance assessment of copper, mild steel, and aluminum alloy 2024-T3 in acidic solution by a novel imidazothiazole derivative, Mater. Today Sustain. 24 (2023) 100524, https://doi.org/10.1016/j.mtsust.2023.100524.